



Sensing and Control Integration for Thrust Vectoring in Heavy UAVs: Real-World Implementation and Performance Analysis

Mohammad Sadeq Ale Isaac ^{ID*}[†], Pablo Flores Peña ^{ID†§}, Marco Andrés Luna ^{ID*}, Ahmed Refaat Ragab ^{ID†‡§}, Pascual Campoy ^{ID*||}

^{*}Computer Vision and Aerial Robotics Group,
Centre for Automation and Robotics (CAR),
Universidad Politécnica de Madrid (UPM-CSIC),
28006 Madrid, Spain

[†]Department of Electrical Engineering,
University Carlos III of Madrid, 28919 Leganés, Spain

[‡]Department of Network,
Faculty of Information Systems and Computer Science,
October 6 University, Giza 12511, Egypt

[§]Drone-Hopper Company, 28919 Leganés, Spain

Unmanned Aerial Vehicles (UAVs) have garnered significant attention among researchers due to their versatility in diverse missions and resilience in challenging conditions. However, electric UAVs often suffer from limited flight autonomy, necessitating the exploration of alternative power sources such as thermal engines. On the other hand, managing thermal engines introduces complexities and internal uncertainties into the system. In this paper, an Adaptive Robust attitude controller (ARAC) is proposed to address these challenges by drawing inspiration from helicopter solutions while minimizing mechanical intricacies. Specifically, the designed algorithm employs Thrust Vector Control (TVC) for an industrial heavy Multi-Ducted Fan (MDF), known for its superior static stability compared to conventional ducted fans. Subsequently, an integrated flap vanes system is positioned at the exhaust of the ducts for precise attitude control, effectively removing unwanted yaw moments associated with traditional propellers. This research builds on prior authors' works to establish a proper mathematical and aerodynamic model. Also, using former simulation results to conduct real flight experiments aimed at enhancing TVC functionality. The findings highlight the effectiveness of this approach for heavy UAV applications. It is worth noting that the practical value of this research lies in its potential to significantly extend flight autonomy supplied by thermal engines and improve the resilience of UAVs in challenging real-world missions. This is particularly achievable provided that the design of flap vanes aligns closely with the dimensions of the duct system, offering a promising solution to a critical engineering challenge in the field of UAV technology.

Keywords: Adaptive sliding mode control; thrust vector control; attitude control; servo flap sensing; heavy UAVs; multi-ducted fan.



Received 12 November 2023; Revised 1 April 2024; Accepted 1 April 2024; Published 4 June 2024. This paper was recommended for publication in its revised form by editorial board member, Swee King Phang.

Email Addresses: ^{*}mo.aleisaackhoueini@upm.es, ^{||}pascual.campoy@upm.es

^{||} Corresponding author.

This is an Open Access article published by World Scientific Publishing Company. It is distributed under the terms of the [Creative Commons Attribution-NonCommercial 4.0 \(CC BY-NC\) License](#), which permits use, distribution and reproduction in any medium, provided that the original work is properly cited and is used for non-commercial purposes.

1. Introduction

During the 20th century, the concept of unmanned aerial vehicles (UAVs) or drones emerged as aircraft that operated without human pilots or crew members on board. Originally, UAV or Remotely Piloted Aerial Vehicles (RPAV) was coined and developed for military aviation, which became widely used to describe such aircraft. However, its application has since expanded beyond the military and into civilian domains. To encompass the complexities of the entire system, the terminology evolved from UAV to Unmanned Aerial System (UAS). The UAS concept incorporates not only the UAV itself but also the Ground Control Station (GCS), communication systems, and networking components [1]. The Federal Aviation Administration (FAA) and the United States Department of Defense (DOD) adopted the terms UAS and Remotely Piloted Aerial System (RPAS) in 2005 to outline their UAS roadmap until 2030 [2]. UAVs can be operated remotely through human piloting or can possess varying degrees of autonomy with the assistance of an Autopilot (AP), ranging from semi-autonomous to fully autonomous capabilities [3, 4].

Additionally, a Ducted Fan (DF) or Ducted Propeller (DP) refers to a mechanical fan or propeller installed inside a cylindrical duct or shroud. This configuration, as studied in the previous research [5, 6], allows for the enhancements to create a Multiple Ducted Fan (MDF) system. The MDF system incorporates a coherent geometry that optimizes the arrangement of DFs to generate the necessary thrust force during flying missions. Depending on their installation direction, DFs can function as longitudinal or vertical thrusters. To meet specific output requirements, DFs undergo optimizations based on factors such as inlet arc shape, duct wall length, and outlet-to-inlet area ratio. These considerations ensure the DFs are precisely designed for optimal performance and efficiency. The integration of DFs and the utilization of MDF systems contribute to advancements in aerospace engineering, enhancing thrust generation and maneuverability in various flight scenarios.

UAVs have garnered great attention from researchers thanks to their wide-ranging applications and exceptional performance capabilities. These versatile aircraft have found extensive utility in both civil and military domains, delivering groundbreaking solutions while minimizing risks for operators. In the civil sector, UAVs have proved invaluable in aerial photogrammetry and videography, cultivation analysis and crop monitoring, firefighting, search and rescue operations, infrastructure inspection, and environmental monitoring. In the military realm, they have diverse applications such as surveillance and reconnaissance, target acquisition and object tracking, battlefield support, and combat operations [7]. Furthermore, the emergence of Vertical Takeoff and Landing (VTOL) systems,

particularly the promising MDFs, has added another dimension to their attractiveness, offering enhanced agility, stability, and versatility for a wide range of applications. Specifically, heavy clusters of UAVs are spread in myriad applications such as firefighting, large package delivery, agricultural protection, passenger transportation, communicative portable stations, and military patrol. Attending such beneficial aerial systems in the industry requires high stability and safe flights, especially in the case of human carriage. Meanwhile, to satisfy the mentioned applications, long-range and high-endurance platforms will be aimed; consequently, heavy drones necessitate quite a lot of power to serve long missions.

UAVs can be classified based on various factors and their extensive usage. These classifications include weight-based, mission-based, flight endurance or range-based, payload-based, and more. Among these, the weight and payload capacity of UAVs plays a significant role in their categorization. According to research in [8, 9], UAVs are categorized as micro, small, medium, and large-scale platforms. In the European Union aviation safety regulations, weight classifications are defined as Class A1 (less than 900 g), Class A2 (less than 4 kg), Class A3 (less than 25 kg), and additional categories for weights exceeding 25 kg. Similarly, the global NATO-STANAG 4670 UAS category classifies UAVs as nanoscale (less than 250 g), microscale (less than 2 kg), small scale (less than 25 kg), medium scale (less than 150 kg), and large scales (more than 150 kg) [10, 11]. Denoting that larger UAVs offer the advantage of carrying heavier payloads over longer distances, While mini-scale UAVs have considerable limitations in terms of flight endurance and payload capacity.

Improving a DF to MDF has several merits, including much more static and dynamic stability due to moving the COG toward a point in the middle of DFs and higher thrust power to carry heavier payloads. To this end, some research focused on controlling MDFs, as the study outlined in [12], researchers focused on a triangular EDF system, focusing on TVC as a critical stabilizing factor. Employing a linear cascade controller, they achieved stable hover performance with minimal disruptions, efficiently regulating angular rates at high frequencies. The controller was split into two components: an onboard gyroscope for real-time angular rate measurement and an offboard calculation module for position and attitude control. Communication with the PX4 autopilot ensured coordination. Notably, mounting the motor controller (YGE 90HV) at the exit nozzle provided cooling through airflow. However, this work primarily relied on controlled settings with motion capture, potentially limiting real-world applicability. Offline primary controller components posed vulnerability to delays or data loss due to connection issues. Battery reliance led to constrained operational times for energy-intensive DFs. While hover

stability was validated, further exploration of diverse flight maneuvers remains a promising avenue.

In a recent study [13], a comprehensive backstepping control approach was introduced, focusing on the trajectory tracking control of a multirotor. This control strategy addressed several intricate challenges, including cascade constraints, constrained actuator dynamics, and complex unknowns. It achieved robustness by integrating sliding mode and dynamics surface control techniques. The researchers decomposed the entire system into five cascade subsystems connected through intermediate nonlinearities. To deal with complex unknowns, they employed adaptive compensators, and through Lyapunov synthesis, they verified minimal errors. While this work provides valuable insights into control methodologies, its application has been primarily limited to simulations and electrical motors.

However, the study in [14] placed a strong emphasis on model predictive and robust model predictive algorithms in the context of DF applications, particularly when dealing with internal uncertainties and external disturbances. Their approach involved addressing a nonminimum phase nonlinear system dynamics and deploying a compound controller designed for both trajectory tracking and attitude control. Similarly, the research presented in [15] delved into the development of a TVC algorithm tailored for a tilt-rotor UAV, even in the presence of actuation constraints. Their simulation methodology prominently featured an infinity curve for applying maximum tilt angles to achieve precise objective tracking. Furthermore, the work in [16] showcased a novel integration of the backstepping technique and fast terminal sliding mode control to govern yaw and tilting angles. These angles were accurately estimated using a robust adaptive backstepping controller within the context of a position controller for path-tracking applications. It is important to note that, similar to previous studies, these investigations have primarily focused on electrical power supply and simulation results.

Whereas in distinct research [17], a comprehensive simulation methodology for a Tandem Ducted Fan (TDF) system is presented, encompassing intricate considerations of aerodynamic interactions and the mathematical underpinnings of flap vanes. This simulation was realized using MATLAB Simulink, offering a versatile and modular framework for TDF analysis. Delving into the intricacies of airflow dynamics within the duct, the study scrutinized the destabilizing effects on the nose-down pitching moment during the transition from edge-wise to axial flight modes at low velocities. By fine-tuning the deflection angle of the vanes, the researchers reported enhancements in transient behavior. This work contributes significantly to theoretical insights and aerodynamic investigations of MDFs, especially those akin to the Urban Aeronautics X-Hawk and the 29-inch UAV, which served as inspirational sources; however,

its real-world applicability might necessitate further implementation beyond the confines of the simulation environment.

In recent studies, [14, 18–21], researchers have extensively explored enhancing the control strategies of Single Ducted Fans (SDFs) using Adaptive Model Predictive Control (AMPC) and an Adaptive Fault-Tolerant approach. The primary objective has been to elevate the performance of SDFs in both transient and cruise modes. The first study introduces a novel control mechanism designed for a specialized DF aerial robot, focusing on fault tolerance against partial actuator failure. This mechanism integrates an identified state-space model in the frequency domain, an adaptive loop coupled with an estimator, and a reconfigurable adjustment law. This combination allows for the estimation and compensation of varying degrees of failure. The effectiveness of the proposed algorithm is validated through both theoretical simulations and real-time flight experiments. The second study explores an AMPC strategy tailored for engine-driven DF lift systems. This approach utilizes a global network model, trained offline with data from a general mean value engine model for two-stroke aviation engines. The constructed network serves as an adaptive, robust, and efficient prediction model for model parameters. The efficiency of this approach is demonstrated through numerical simulations depicting a vertical take-off thrust preparation process for the DF lift system. While these studies demonstrate the controller's effectiveness in stabilizing drones during real flights, a significant challenge remains in dealing with the inherent dynamics and instability characteristic of single DFs. While, this paper addresses the stability issues by introducing a hexa model, co-located to work in conjunction with the SDF. The combined configuration is designed to compensate for both transient and cruise flight dynamics. Additionally, the proposed approach aims to enhance the payload capacity, a task challenging to achieve with single DFs alone.

In a related study, discussed in [22], researchers focused on an MDF flying object consisting of two EDFs connected by a vertical wooden bar. The unique feature of their design was the rotatable installation of the EDFs, functioning like a hinge to induce roll, pitch, and yaw rotations. Employing a PD controller initially, the system encountered a persistent steady-state error, prompting the integration of an integral term, which effectively mitigated this error. While the effort showcased valuable insights, the positioning of the battery and equipment on the wooden bar introduced an imbalance by shifting the COG to a higher point relative to the EDF plane. This configuration likely contributed to the observed steady-state error. Furthermore, the study highlighted a limitation in endurance, attributed to the low battery capacity not suitable for powering two EDFs.

However, in another research [23], the authors proposed a novel TDF for drones, featuring small EDFs and larger TDFs controlled by a robust static H_∞ output feedback technique. The controller effectively stabilizes and decouples body-frame velocities and yaw angle states, even in the presence of disturbances and EDF tilting. The study also addresses time delays caused by open-loop gain roll-off using system identification. However, the approach's applicability to industrial platforms is limited due to component disharmony and complexities associated with decoupling.

In a relevant study [24], a compact MDF was introduced, utilizing two DFs for vertical stabilization and two EDFs for attitude control. The study employed a structured multi-loop feedback attitude controller based on H_∞ synthesis, encompassing a low-order attitude controller and multi-loop feedback for cross-attitude decoupling and reference signal tracking. Controller parameter tuning was conducted using a nonsmooth optimization method. Although the approach demonstrates promise, further investigation is recommended to address significant uncertainties, disturbances, or actuator/sensor faults, as also asserted by the authors.

Moreover, the advancements in intelligent health management methods for complex mechanical gear systems in DFs can significantly enhance their operational reliability. The work done in [25, 26], which employs a digital twin-driven methodology for gear surface degradation assessment, provides valuable insights into predictive maintenance and real-time system assessment. The ability to automatically establish high-fidelity digital twin models that reflect dynamic responses is akin to the development of digital twins for DF systems, where real-time modeling can be crucial for precise attitude control and stability. The use of transfer learning and advanced signal processing methods, as explored in their research, can have parallels in the development of control algorithms, ensuring efficiency even in the presence of wear-related changes. Furthermore, their emphasis on the broader applicability of digital twin techniques in industrial practices aligns with enhancing DF control methods for heavy UAV applications.

On the other hand, to choose appropriate engines and meet power requirements, a delicate balance must be struck when selecting the engine and fuel type. As discussed in [27], combustion engines remain a popular choice for both commercial and private applications, despite their lower efficiency compared to more reliable electrical counterparts. Electric power supply units (PSUs) boast high density but are sensitive to water or vapor and exhibit limited recharge cycles, making them less suitable for large-scale flying drones. Hydrogen fuel cells (HFCs) offer renewable energy with remarkable endurance, producing 150 times the energy of Li-Po batteries in fixed-wing aircraft. However, their reliance on a rapid-response

hydrogen setup limits their affordability. Uninterruptible power sources (UPS) via cable are effective for near-ground tests and emergency landings but impractical for long-range flights [28]. Considering the advantages and disadvantages of various power sources in terms of engine efficiencies, fossil fuels emerge as a concentrated and cost-effective choice, easily accessible and capable of providing substantial energy for extended flight durations. In contrast, a myriad of engine types can be considered, powered by chemical, electrical, and nuclear energy. These include heat engines, electrical engines, disk engines, nuclear propulsive, hybrid propulsive, jet propulsive, and ion propulsive engines [29]. Electric engines demonstrate rapid acceleration and operational efficiency but require a continuous power supply, making them unsuitable for prolonged flights. Heat engines encompass both internal and external combustion engines, featuring variations such as piston, rotary, jet, and ion engines. The piston engine, particularly in two- and four-stroke configurations, is conventional and distributed in Wankel, dual-fuel, and other setups. While these engines exhibit high power-to-weight ratios, they tend to be noisier than electric alternatives. Focusing on internal combustion engines, two- and four-stroke categories stand out. The latter, despite having a lower power-to-weight ratio than its counterpart, proves more compatible with heavy drones due to distinct lubrication setups that eliminate the oil-fuel mixture. This advantage allows four-stroke engines to operate effectively at higher altitudes. While they are slightly heavier due to additional moving components, their reliability and economic efficiency make them a preferable choice among various engine types. In conclusion, this paper has opted for an industrial internal combustion engine arrangement, employing three engines consecutively to drive the six propellers. Each pair of propellers is dedicated to a thermal engine, ensuring a continuous rotation to maintain equal thrust. This distribution is selected to address the inherent delay thermal engines face in responding to different rotation requirements compared to electrical engines. Despite this drawback, if all motors consistently receive the same command with a simultaneous and constant change, the delay becomes negligible. Moreover, the system incorporates an industrial Engine Control Unit (ECU) to effectively regulate the parameters of the engines.

Addressing thermal engine instabilities, this paper focuses on the control solution to achieve extended autonomy while regulating uncertainties, building upon the authors' previous research presented in [8, 9, 30]. In this section and prior research, a variety of control solutions for DF applications have been explored, encompassing nonlinear methods, [14–16, 24, 27, 31–33], linear approaches like Proportional-Integral-Derivative (PID) control (PID) or cascade PIDs [12, 17, 22, 34], feedback linearization [23], and linear-quadratic regulator [35]. However, it is

noteworthy that there have been limited industrial efforts directed toward real-flight implementations of TVC for heavy multi-UAVs. The scarcity of such initiatives can be attributed to the challenges of translating theoretical techniques into practical reliability due to the numerous unknown uncertainties inherent in real-world scenarios, leading the industry to rely heavily on conventional PID controllers. This paper addresses this gap by introducing a fine-tuned compound controller, previously deployed on smaller platforms like the Fan Hopper [8], and enhancing its performance against external nonlinearities.

Building upon the comparison results discussed in [8, 9, 30], this paper distinctly focuses on real-world experiments, culminating in a final simulation step with fine-tuned controller parameters, comparing the Adaptive Robust attitude controller (ARAC) results to one conducted by a well-tuned PID controller. The contributions of this paper can be summarized as follows:

Refinement of Mathematical Model: The mathematical model previously introduced in [30] for a similar drone application is refined and optimized specifically for heavy drone applications. This refinement contributes to a more accurate representation of the system dynamics.

Enhancement of Robust Controller: The robust controller presented in [9] undergoes improvement through parameter tuning for both stationary and real flights on an industrial autopilot application. Additionally, an adaptive component is integrated into the controller, enhancing system reliability against internal nonlinearities and external disturbances.

Real Flight Conduct: After meticulous parametric refinement of the adaptive controller introduced in [8], taking into account fluid payload uncertainties impacting the overall UAV mass, the modeled system was subjected to real flight experiments. This phase aimed to assess the controller's performance in practical scenarios and identify areas for further enhancement.

By concentrating on these three key aspects, this paper advances the field by addressing experimental challenges and refining the ARAC methodologies for enhanced performance in real-world applications. The term ARAC embodies the fusion of two distinct systems: the adaptive controller, comprehensively discussed in [8], and the robust controller, detailed in [9]. While the latter paper showcases the ability to maintain the stability of a medium-scale hexa DF system, particularly when carrying a liquid payload that introduces nonlinearities and additional degrees of freedom during maneuvers or release phases, the former paper focuses on reinforcing the controller system against external uncertainties, such as wind disturbances. This paper takes a step further by integrating these two algorithms, refining the controller parameters, and constructing a robust

algorithm capable of mitigating both internal and external uncertainties. This amalgamation aims to enhance the overall performance of the ARAC, offering a practical solution to challenges posed by various operational conditions.

The proposed solution involves the implementation of an ARAC to actuate the servo flaps on the control surfaces, improving the regulation of the multi-ducted fan's attitude. To achieve this goal, the robust algorithm harnesses the power of Sliding Mode Control (SMC) to counteract wind disturbances effectively. While SMC is a well-established methodology, this research introduces vital adaptations and refinements specifically tailored to confront the unique challenges experienced in real-flight applications. This endeavor entails sophisticated modifications aimed at mitigating the inherent complexities associated with a system of this magnitude and nature. Moreover, the adaptive aspect of this approach plays a pivotal role in managing internal nonlinearities induced by combustion engines, effectively addressing issues like undesired vibrations that are, at times, inevitable in such engine operations. Additionally, the exploration of TVC within this framework is driven by the need to provide a stable attitude controller among a few possible solutions for UAVs supplied by thermal engines. While TVC is not a novel concept itself, this presents innovative strategies for applying TVC to achieve optimal attitude control, particularly using flap vanes.

2. Sensor Integration Review

This paper consolidates the outcomes of three prior research endeavors conducted by the authors, offering a concise review to elucidate the progression of work and the evolution of prototypes in each study. Commencing with an exploration into the domain of MDFs, our initial undertaking involved the meticulous construction of a scaled-down prototype. As an initial step towards delving into the realm of MDFs, a scaled-down prototype was meticulously crafted. This prototype served as a valuable tool for gaining deeper insights into the intricate dynamics of EDFs and exploring the realms of stability enhancement to optimize controller performance, as delineated in [8]. Thus, the meticulously tailored MDF, referred to as "FAN HOPPER" in this publication, boasts distinctive attributes, which are briefly enumerated in what follows:

FAN HOPPER: It embodies a 6DOF hexa MDF system, leveraging electric propulsion technology that emulates the operational characteristics of conventional thermal engines. This design choice provides an avenue to explore and address the inherent uncertainties reminiscent of thermal motors within this context. Rigorous aerodynamic analyses

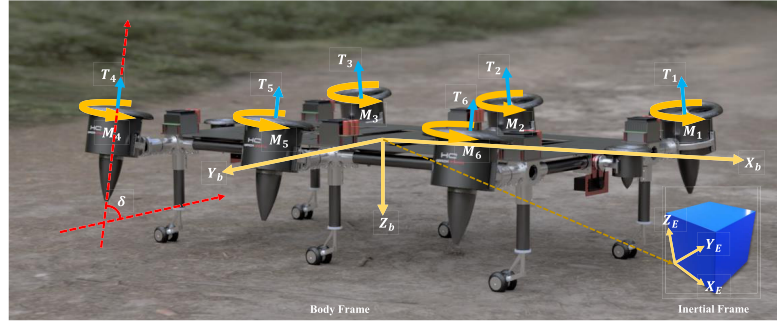


Fig. 1. The general coordinate system based on the FAN HOPPER prototype; T_i and M_i are thrusts and moments generated by the EDFs, δ is the Angle of Incidence (AOI) of EDFs according to experiment, $\{\}_b$ is the subscript for the body-fixed frame, and $\{\}_E$ is the subscript for the inertial frame.

were conducted, leading to significant enhancements across the entire platform. Notably, the innovative duct design yielded multiple benefits, including the attainment of a streamlined inlet and outlet airflow even at elevated horizontal velocities. Moreover, a remarkable reduction in undesired yaw moments, historically associated with instability in high-powered multi-rotor propellers, was observed. This achievement is particularly noteworthy as the constrained space between the duct wall and the rotor blades virtually eliminates yawing, thereby contributing to enhanced stability. Consequently, the consideration of rotor rotation direction becomes superfluous, and as illustrated in "Fig. 1", the EDFs exhibit uniform rotation due to their near-zero yawing moments. Furthermore, as depicted in the figure, empirical investigations led to the incorporation of an optimized Angle of Incidence (AOI), enhancing stabilization during yawing. This concept is further described in [8], providing a better insight into its implementation and impact.

In the next step, a significant milestone was achieved by developing a larger-scale prototype intended to be fitted with thermal engines, thereby advancing toward the

ultimate objective. This design endeavor was fortified by meticulous modeling, expounded upon in [30], which furnished a comprehensive mathematical representation of the dynamic system governing the extensive MDF. Noteworthy traits of this UAV, dubbed "DUTY HOPPER," are briefly outlined as follows:

DUTY HOPPER: It is a 6DOF quad MDF system harnessing thermal propulsion technology through the integration of two longitudinally aligned motors. This configuration also boasts the capability to accommodate Lipo batteries for supplementary attitude stabilization. Detailed in [30], it marked the pioneering instance of laboratory modeling and design. Subsequently, to enhance controller performance, several tests were conducted, including the incorporation of diverse payloads (solid and liquid), culminating in the development of a standardized prototype. By utilizing thermal engines, this platform obviates the need for ESCs in the main ducts, instead adopting an ECU system to translate AP commands for propeller control and maintain a consistent angular velocity across all propellers using a simple PID for different RPM bounds, ensuring safe takeoff and landing. Attitude regulation is achieved via flap vanes, as depicted in

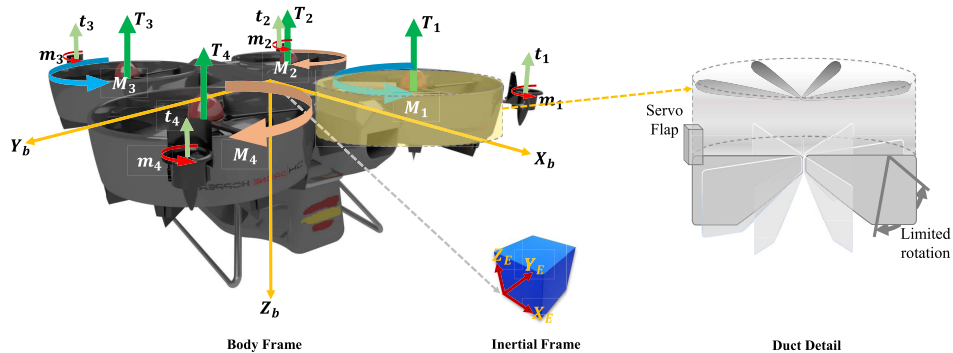


Fig. 2. The general coordinate system based on the DUTY HOPPER prototype; T_i and M_i are thrusts and moments generated by the main ducts, t_i and m_i are thrusts and moments generated by the EDFs, $\{\}_b$ is the subscript for the body-fixed frame, and $\{\}_E$ is the subscript for the inertial frame.

"Fig. 2", wherein commanded surge, sway, and heave movements are doubly derived to suitably control Euler angles ϕ , θ , and ψ . Furthermore, "Fig. 2" shows the configuration of each duct, the inlet airflow, and a schema of rotational flap vanes, which are unveiled in [9]. Notably, based on experimental findings, each flap's rotation is constrained within a $\pm 15^\circ$ range to avert mechanical interference with other flap rotations during both modeling and operational phases.

In the third stage, a synthesis of the preceding experiments led to the development of an advanced, larger-scale prototype tailored for integration with thermal engines. The comprehensive evolution encompassing enhanced modeling, refined control algorithms, and meticulous simulations culminated in [9]. This iteration witnessed significant advancements in power supply, safety measures, communication systems, auxiliary EDF concepts, and overall geometry. Aptly named "WILD HOPPER," this ultimate prototype encapsulates these refinements in a coherent design as follows.

WILD HOPPER: It is a hexa MDF platform featuring 6 DOF, equipped with six main ducts and four auxiliary EDFs for safety and emergencies, as elaborated in [9]. This prototype operates on two power sources: primary propellers are fueled by thermal energy, while EDFs are powered by Lipo batteries. The payload compartment can handle up to 60% of the total weight. The configuration, depicted in "Fig. 3", outlines forces, moments, rotations, movements, and frame connections between the **BFF** and **Inertial Frame**. The model has been extensively enhanced. Notable improvements include refining the aerodynamic model with blade tip angle adjustments and blade count optimization for superior thrust. The communication system received upgrades, incorporating redundancy for reliable short and long-distance links. Employing a TVC strategy, the control system employs geometrically enhanced flap vanes as control surfaces, evolved iteratively during the design.

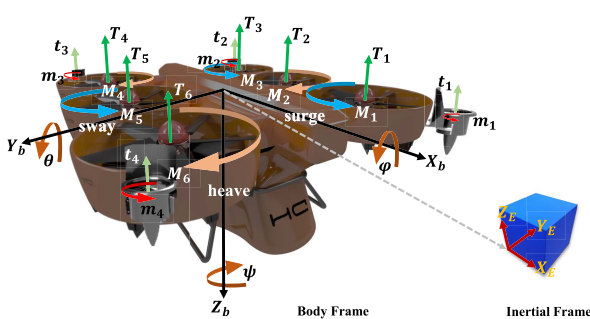


Fig. 3. The general coordinate system based on the final WILD HOPPER prototype; T_i and M_i are thrusts and moments generated by the main ducts, t_i and m_i are thrusts and moments generated by the EDFs, $\{\cdot\}_b$ is the subscript for the body-fixed frame, and $\{\cdot\}_E$ is the subscript for the inertial frame.

3. Methodology

The research methodology employed through this paper and previous works [8, 9, 30] can be classified as *Applied Research* [36], which differentiates the context from fundamental (basic) research in terms of purpose, context, and methods. Applied research aims to solve practical problems, whereas basic research seeks to study certain issues without immediate practical application. Specifically, the objective followed in this paper is to compound the control algorithms proposed in prior works and improve the controller parameters to provide a fine-tuned robust controller with optimized performance for a real industrial application. The key elements of this paper are elaborated as follows:

- **Purpose:** Solve the mathematical modeling and dynamics of heavy MDF UAVs while applying flap vanes to stabilize the attitude using Adaptive Sliding Mode Control (ASMC) and enhance the control issue by implementing TVC using flap vanes. In previous works, the focus was on solving the control issue defined previously in simulation and smaller prototypes for evaluating the controller's performance under motor failure and external noises.
- **Context:** The context of this paper is highly valuable due to the industry's long-standing need for easy-to-set-up UAVs that can carry heavy payloads for extended flight autonomy. This requirement is addressed in the aforementioned works, where a system is developed to supply thermal energy for extended flight autonomy and equipped with a controller that avoids mechanical complexities and is rational for such a system.
- **Methods:** The methods used in the whole work involve advanced control algorithms, particularly SMC, applied in a novel way to achieve TVC using flap vanes. The design is easily extendable for similar platforms, and the application of SMC offers the advantage of easy tuning compared to conventional PID controllers.

Furthermore, the methodology utilized in this paper is a combination of the system engineering method derived from the system engineering process organized in [37]. This process is abbreviated as "S.I.M.I.L.A.R." and encompasses the following steps: State the problem, Investigate alternatives, Model the system, Integrate solutions, Launch the system, Assess performance, and Reevaluate, which are shown in "Fig. 4":

4. Advanced Control Algorithm Integration for Attitude Stability

In Sec. 2, the three stages of development were reviewed and culminated in the creation of the final integrated model.

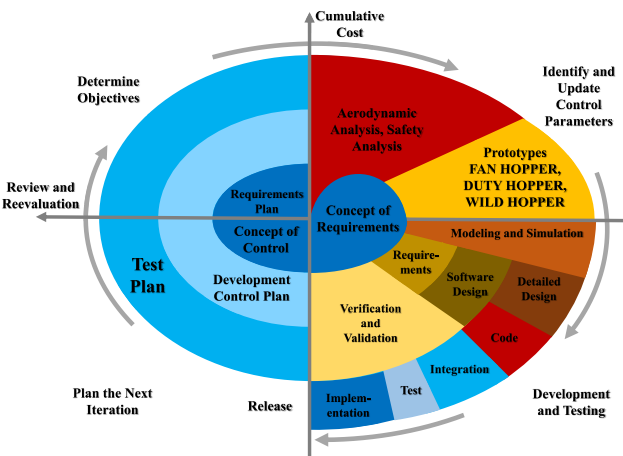


Fig. 4. Methodology approach model followed in this paper, according to the “S.I.M.I.L.A.R.” [37], and the spiral procedure defined in [38].

This model integrates a complex control algorithm that merges Model Reference Adaptive Control (MRAC) and SMC methodologies, giving rise to an ASMC approach. By leveraging the MRAC algorithm outlined in a prior publication [8], along with the acquired parameters and the SMC parameters fine-tuned in this research, this novel approach has demonstrated remarkable efficiency in addressing the internal and external nonlinearities encountered during UAV operations. It utilizes a Lyapunov candidate to provide strong stability assurances, enhancing the overall stability and control of the UAV system. For ease of understanding, this section is divided into two parts: Enhanced dynamic model and advanced attitude controller.

4.1. Enhanced dynamic model

Given the 6DOF rigid body of an MDF as a complex Multi-Input Multi-Output (MIMO) system due to its nonlinear configuration, the governing equations can be derived from the Newton–Euler equation set. These equations are formulated with respect to either the **Body-Fixed Frame (BFF)** or **Earth-Fixed Frame (EFF)**, which are denoted as subscripts $\{\cdot\}_b$ and $\{\cdot\}_e$, respectively.

$$\begin{aligned}
 \mathbf{v}_b &= [u \ v \ w]^T, \\
 \boldsymbol{\omega}_b &= [p \ q \ r]^T, \\
 \mathbf{I}_b &= \begin{bmatrix} I_{xx} & 0 & 0 \\ 0 & I_{yy} & 0 \\ 0 & 0 & I_{zz} \end{bmatrix}, \\
 \mathbf{F}_b &= F_{\text{grav}} + F_{\text{fuse}} + F_{\text{prop}} + F_{\text{duct}} + F_{\text{edf}} + F_{\text{fv}}, \\
 \mathbf{M}_b &= M_{\text{gyro}} + M_{\text{prop}} + M_{\text{duct}} + M_{\text{edf}} + M_{\text{fv}}, \\
 \dot{\mathbf{v}}_b &= -\boldsymbol{\omega}_b \times \mathbf{v}_b + \frac{1}{m_b} (\mathbf{F}_b + F_{\text{grav}}), \\
 \dot{\boldsymbol{\omega}}_b &= \mathbf{I}_b^{-1} (\mathbf{M}_b - \boldsymbol{\omega}_b \times \mathbf{I}_b \times \boldsymbol{\omega}_b),
 \end{aligned} \tag{1}$$

it is worth noting the distinction between F_{prop} and F_{duct} , which may initially seem equal, but they serve distinct roles, and both contribute to force generation in the BFF. This distinction is as follows.

Propeller Thrust (F_{prop}): The primary thrust in a DF system originates from the propeller or fan itself. As the fan’s blades rotate, they create an airflow that generates thrust by propelling the air in the opposite direction, by Newton’s third law of motion. This thrust is the central driver of propulsion.

Duct Thrust (F_{duct}): The duct that surrounds the fan plays a critical role in optimizing the propeller’s performance. By guiding and channeling the airflow generated by the fan, the duct minimizes air loss and enhances the system’s overall efficiency. While the duct does not generate thrust in the same direct manner as the propeller, its design significantly influences the system’s total thrust generation, which is elaborately discussed in [30].

Subsequently, translating the velocities and attitudes between the BFF and the Inertial frame yields:

$$\begin{aligned}
 \mathbf{r} &= [x \ y \ z]^T, \\
 \boldsymbol{\alpha} &= [\phi \ \theta \ \psi]^T, \\
 \mathbf{C}_{eb} &= \begin{bmatrix} c(\psi)c(\theta) & c(\psi)s(\theta)s(\phi) & c(\psi)s(\theta)c(\phi) + s(\psi)s(\phi) \\ s(\psi)c(\theta) & s(\psi)s(\theta)s(\phi) & s(\psi)s(\theta)c(\phi) - c(\psi)s(\phi) \\ -s(\theta) & c(\theta)s(\phi) & c(\theta)c(\phi) \end{bmatrix}, \\
 \mathbf{v}_e &= [\dot{x} \ \dot{y} \ \dot{z}]^T = \mathbf{C}_{eb} \mathbf{v}_b, \\
 \dot{\boldsymbol{\alpha}} &= \begin{bmatrix} 1 & s(\phi)t(\theta) & c(\phi)t(\theta) \\ 0 & c(\phi) & -s(\phi) \\ 0 & s(\phi)/c(\theta) & c(\phi)/c(\theta) \end{bmatrix} \boldsymbol{\omega}_b,
 \end{aligned} \tag{2}$$

In “Eqs. (2)”, the symbol \mathbf{r} represents the location vector observed in the EFF, while \mathbf{C}_{eb} stands for the rotation matrix that corresponds to the airframe’s yaw, pitch, and roll transformations from the Earth-Fixed Frame to the BFF. This pivotal matrix is known as the Direction Cosine Matrix (DCM). The functions $s()$, $c()$, and $t()$ signify the sine, cosine, and tangent functions, respectively. The symbol $\boldsymbol{\alpha}$ refers to the Euler angles vector, while \mathbf{v}_e represents the velocity vector in the EFF, which is equivalent to the velocity vector in the BFF after being multiplied by the rotation matrix. Additionally, the time derivatives of the Euler angles are determined by the angular velocity in the BFF and are multiplied by the rotational matrix to account for the transformation.

By substituting the moments into the Newton–Euler equation, the specified dynamic equations can be

determined. Further, the rotation dynamics equations can be obtained by considering the acceleration in EFF and the BFF, resulting in

$$\begin{aligned}
 \mathbf{F}_b &= [F_{bx} \ F_{by} \ F_{bz}]^T, \\
 \mathbf{M}_b &= [M_{bx} \ M_{by} \ M_{bz}]^T, \\
 \mathbf{F}_{bx} &= m_b(\dot{u} + gs(\theta) + qw - rv), \\
 \mathbf{F}_{by} &= m_b(\dot{v} - gc(\theta)c(\phi) + ru - pw), \\
 \mathbf{F}_{bz} &= \mathbf{F}_b - m_b(\dot{w} - gc(\theta)c(\phi) + pv - qu), \\
 \mathbf{M}_{bx} &= I_x\dot{p} + (I_z - I_y)qr - I_p\omega_pq, \\
 \mathbf{M}_{by} &= I_y\dot{q} + (I_x - I_z)rp + I_p\omega_pp, \\
 \mathbf{M}_{bz} &= I_z\dot{r} + (I_y - I_x)pq + I_p\dot{\omega}_p - Q, \\
 \rightarrow \dot{\omega}_b &= [\dot{p} \ \dot{q} \ \dot{r}]^T \\
 &= \begin{pmatrix} ((I_y - I_z)qr + I_p\omega_pq + \mathbf{M}_{bx})/I_x \\ ((I_z - I_x)rp - I_p\omega_pp + \mathbf{M}_{by})/I_y \\ ((I_x - I_y)pq - I_p\dot{\omega}_p + \mathbf{M}_{bz} + Q)/I_z \end{pmatrix}, \\
 \rightarrow \dot{\mathbf{v}}_b &= [\dot{u} \ \dot{v} \ \dot{w}]^T \\
 &= \begin{pmatrix} \mathbf{F}_{bx}/m_b - gs(\theta) + rv - qw \\ \mathbf{F}_{by}/m_b + gc(\theta)c(\phi) + pw - ru \\ (\mathbf{F}_b - \mathbf{F}_{bz})/m_b + gc(\theta)c(\phi) + qu - pv \end{pmatrix}
 \end{aligned} \tag{3}$$

Through "Eqs. (3)", the symbols I_p and ω_p refer to the inertia and angular rate of the propellers, respectively. Additionally, M_{bx} , M_{by} , and M_{bz} represent the moments along different axes in the BFF, while F_{bx} , F_{by} , and F_{bz} denote forces on the corresponding coordinate axes in the BFF. The term Q denotes the propeller's anti-torque, and g represents the gravitational acceleration.

Hence, as the analysis delves into the dynamic equation, it considers the presence of a duct, examining the

aerodynamic interactions with it and the turning effects induced by the propeller, as illustrated in Fig. 5.

Figure 5 provides a visual representation of the various stages of the free airstream as it traverses through a duct. These stages encompass the upstream, propeller inlet, outlet, and downstream portions. Subscripts $\{\}_0$ correspond to the upstream airflow well before it enters the duct, $\{\}_i$ pertains to the inlet airflow, $\{\}_e$ signifies the exit or outlet airflow, and $\{\}_\infty$ represents the downstream airflow much further from the duct. Additionally, α , V , and A , respectively, denote the airflow angle, velocity, and planar area at each stage. Additionally, angles α_i and α_e , corresponding to the airflow angle within the duct inlet and the airflow angle at the outlet of the duct, respectively, can be determined as follows:

$$\begin{aligned}
 \alpha_i &= \alpha_0 + k_i \left(\frac{\pi}{2} - \alpha_0 \right), \\
 \alpha_e &= \alpha_0 + k_e \left(\frac{\pi}{2} - \alpha_0 \right), \\
 \alpha_\infty &= \alpha_0 + k_\infty \left(\frac{\pi}{2} - \alpha_0 \right),
 \end{aligned} \tag{4}$$

In "Eqs. (4)", the terms k_i , k_e , and k_∞ correspond to flow turning efficiency factors influenced by the inlet propeller plane, the outlet plane, and the downstream region far from the duct. It is important to note that in various articles, notably [17, 39–42], a single airflow angle is commonly utilized for both α_e and α_∞ . This approach simplifies the assumption or utilizes an average value for the angle of deflection at a specific downstream point, often situated far from the duct exit. This choice facilitates an understanding of aerodynamic behavior without delving into the intricacies of particular flow interactions. Now, based on the airflow angle at various stages, the velocities at the upstream,

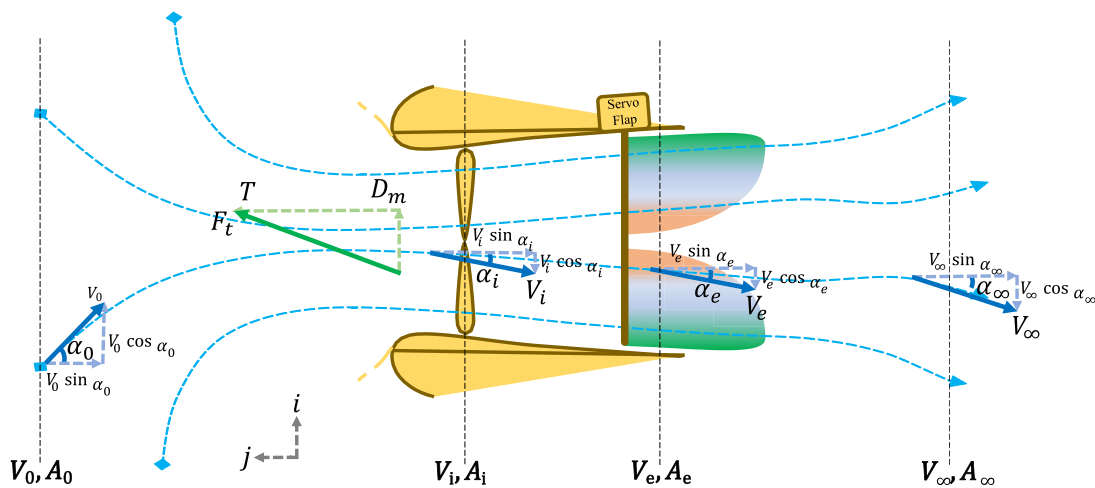


Fig. 5. Schematic of the free airstream passing through a duct, analyzed in four stages: upstream, propeller inlet, outlet, and downstream.

duct inlet, outlet, and downstream can be expressed as follows:

$$\begin{aligned}\mathbf{V}_0 &= V_0 \cos(\alpha_0) \mathbf{i} - V_0 \sin(\alpha_0) \mathbf{j}, \\ \mathbf{V}_i &= V_0 \cos(\alpha_i) \mathbf{i} - (V_0 \sin(\alpha_i) + v_i) \mathbf{j}, \\ \mathbf{V}_e &= V_0 \cos(\alpha_e) \mathbf{i} - (V_0 \sin(\alpha_e) + v_e) \mathbf{j}, \\ \mathbf{V}_\infty &= V_0 \cos(\alpha_\infty) \mathbf{i} - (V_0 \sin(\alpha_\infty) + v_\infty) \mathbf{j},\end{aligned}\quad (5)$$

Using "Eqs. (5)", the terms v_i , v_e , and v_∞ represent the induced speeds caused by the airflow as it passes through the duct. Besides, the induced exit velocity is also well known as slipstream velocity [43]. These speeds are oriented vertically, in the same direction as the vertical axis. Furthermore, as shown in "Fig. 5", the total force vector generated by the duct system is denoted as \mathbf{F}_{t} , which is assumed to comprise a vertical thrust component, T , and a horizontal momentum drag component, D_m . Specifically, T encompasses the combined thrust produced by both the propeller and the duct itself, leading to the equation:

$$\begin{aligned}\mathbf{F}_{\text{duct}_t} &= D_m \mathbf{i} + T \mathbf{j}, \\ \mathbf{T} &= F_{\text{prop}} + F_{\text{duct}} = F_{\text{prop}}(1 + k_{\text{aug}}).\end{aligned}\quad (6)$$

In "Eq. (6)", the symbol k_{aug} denotes the Thrust Augmentation Factor (TAF), which signifies the influence of the duct's lift effect. A TAF value of 1 indicates that the total thrust generated is twice that of the propeller thrust alone. This rationale underscores the selection of the DF model, as it effectively enhances the overall system efficiency. Additionally, when taking into account the airflow mass rate, as well as the horizontal and vertical thrust forces, the following expressions are applicable:

$$\begin{aligned}\dot{m} &= \rho A_i V_i, \\ \mathbf{T} &= \dot{m}(\mathbf{V}_e - \mathbf{V}_0), \\ \xrightarrow{\text{Simplifying}} \mathbf{T} &= \dot{m}(\mathbf{V}_\infty - \mathbf{V}_0), \\ \xrightarrow{\text{Simplifying}} \mathbf{T} &= \dot{m}(\sin(\alpha_\infty) - \sin(\alpha_0)) \mathbf{V}_0 + \mathbf{v}_\infty, \\ \mathbf{D}_m &= \dot{m}(\cos(\alpha_0) - \cos(\alpha_e)) \mathbf{V}_0, \\ \xrightarrow{\text{Simplifying}} \mathbf{D}_m &= \dot{m}(\cos(\alpha_0) - \cos(\alpha_\infty)) \mathbf{V}_0.\end{aligned}\quad (7)$$

Equation (7) are obtained assuming the conservation of energy, momentum, and the mass flow rate from the inlet of the duct to the downstream. ρ is the density of the air-stream, and for simplifying the $\alpha_e = \alpha_\infty$ and $V_e = V_\infty$. Finally, the whole force generated by the duct system is determined as follows:

$$\mathbf{F}_{\text{duct}_t} = 2\rho A_i \left(\frac{1}{1 + k_{\text{aug}}} (V_0 \sin(\alpha_i) + v_i) - V_0 \sin(\alpha_0) \right) \sqrt{V_0^2 + 2V_0 v_i \sin(\alpha_i) + v_i^2}. \quad (8)$$

The total force denoted as $\mathbf{F}_{\text{duct}_t}$ in "Eq. (8)", can also be expressed and simplified in a vectorized manner as follows. Additionally, based on the equations detailed in (1) and described in [30], the remaining forces and moments acting on the BFF can be presented as follows:

$$\begin{aligned}\mathbf{F}_{\text{grav}} &= \begin{bmatrix} -mg \sin \theta \\ mg \cos \theta \sin \phi \\ mg \cos \theta \cos \theta \end{bmatrix}, \\ \mathbf{F}_{\text{fuse}} &= -0.5\rho \begin{bmatrix} C_{D_x} u_b |u_b| A_{\text{side}} \\ C_{D_y} v_b |v_b| A_{\text{side}} \\ C_{D_z} w_b |w_b| A_{\text{top}}, \end{bmatrix}, \\ \mathbf{F}_{\text{prop}} &= 0.5\rho A_i b \Omega_p^2 \begin{bmatrix} C_{D_{bl}} \sin \alpha_{bl} \sin \theta_{bl} \\ -C_{D_{bl}} \sin \alpha_{bl} \sin \theta_{bl} \\ C_{L_{bl}} \cos \alpha_{bl} \cos \theta_{bl} \end{bmatrix}, \\ \mathbf{F}_{\text{duct}} &= D_m + K_{\text{aug}} F_{\text{prop}} = 0.5\rho C_{D_{\text{duct}}} \begin{bmatrix} A_e u_0 |u_0| \\ A_e v_0 |v_0| \\ A_i K_{\text{aug}} V_i |V_i| \end{bmatrix}, \\ \mathbf{M}_{\text{gyro}} &= NJ \omega \begin{bmatrix} -q \\ p \\ 0 \end{bmatrix}, \\ \mathbf{M}_{\text{duct}} &= \begin{bmatrix} F_{\text{duct}_y} r \\ F_{\text{duct}_x} r \\ F_{\text{duct}_z} l_d \end{bmatrix}\end{aligned}\quad (9)$$

In "Eqs. (9)", specific parameters are defined as follows: N represents the number of propellers, J denotes the rotor inertia, while p and q correspond to the angular rates of the propellers discussed in [24, 44]. It is important to note that this equation is applicable when the angular rates are assumed to be semi-constant, irrespective of any aggressive flight behavior. Additionally, C_D stands for the drag coefficient of the fuselage, A_{side} represents the cross-sectional area of the drone, assuming symmetry on both sides and A_{top} denotes the top area of the MDF. The blade pitch is denoted as θ_{bl} , and the blade incidence angle is represented by α_{bl} , which in hover flight conditions, both θ_b and α_b are considered negligible due to their small values. The Ω_p corresponds to the propeller angular velocity, b is the thrust factor of the propeller, and $C_{D_{bl}}$ and $C_{L_{bl}}$ are the drag and lift coefficients of the propeller blades. The parameter $C_{D_{\text{duct}}}$ stands for the duct moment coefficient, serving as a proportionality constant that relates the moment to the dynamic pressure caused by crosswind effects, introduced in [44]. Referring to "Fig. 5", the variables V_0 represent the duct inlet air velocity, r corresponds to the duct exit radius, l_d is the diagonal distance between the Center of Pressure (COP) of the duct to the COG of the MDF, and finally, V_0 , A_i , V_e , and A_e represent the rotor plane and duct exit velocities and areas, respectively.

As depicted in "Fig. 6", the "WILD HOPPER" platform utilizes a hexagonal geometry with a set of vanes positioned at the duct exits. This arrangement consists of 12 pairs of vanes strategically configured for optimal control and effective

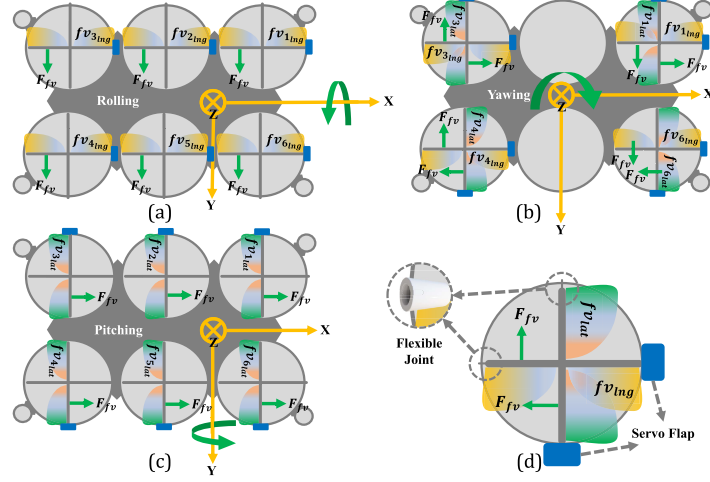


Fig. 6. Top-Down view schematic of 12 pairs of flap vanes on the “WILD HOPPER” prototype, strategically positioned at the duct outlets to generate specific moments: (a) Rolling moment, (b) Yawing moment, (c) Pitching moment. In (d), a detailed view of a single duct featuring two pairs of vanes is depicted.

functionality in influencing a sizeable payload. The term “pair” signifies that each duo of flap vanes is linked by a shaft and managed by a singular servo flap, efficiently rotating both vanes. This configuration offers several advantages: reduced mechanical complexity, simplified control and computation, error prevention, and enhanced moment generation. In this configuration, each duct has two lateral flap vanes, denoted as f_{vlat} , and two longitudinal flap vanes, labeled as $f_{\text{v.lng}}$. In this context, the term f_{v} signifies a flap vane, while $F_{f_{\text{v}}}$ symbolizes the force exerted by a flap vane oriented in the opposite direction of its corresponding azimuthal angle. This phenomenon is also clearly depicted in “Fig. 7”. Additionally, the arrangement of each servo flap is illustrated in “Fig. 6(d)”, showcasing the asymmetrical layout of the servo installations. The decision to employ two servo flaps instead of four is driven by efficiency, as it eliminates the need for disparate angle production and yields more harmonized force generation. This advantageous design choice is further emphasized in the magnified circle adjacent to the duct. A flexible joint is connected to the duct’s wall at the other end of the servo bar, facilitating smooth rotation of the flaps bar under the influence of servo-generated moments.

Explicitly, considering the Wake Skew Angle (WSA) of the airflow, which correlates with α_i , α_e , and α_∞ as depicted in “Fig. 5”. This entails:

$$\begin{aligned} \xi_i &= \arctan \left(\frac{V_0 \cos(\alpha_i)}{V_0 \sin(\alpha_i) + v_i} \right), \\ \xi_e &= \arctan \left(\frac{V_0 \cos(\alpha_e)}{V_0 \sin(\alpha_e) + v_e} \right), \\ \xi_\infty &= \arctan \left(\frac{V_0 \cos(\alpha_\infty)}{V_0 \sin(\alpha_\infty) + v_\infty} \right). \end{aligned} \quad (10)$$

In “Eqs. (10)”, the symbol ξ denotes the WSA, representing the angle that characterizes the skewness of the wake airflow. This angle quantifies the misalignment between the direction of the wake and the flight path of the drone. On the other hand, the high spinning of the propeller induces a drag force, resulting in a swirling motion of the flow. This effect introduces a swirl velocity into the flow, which can be described as follows:

$$\omega_{\text{swirl}} = \frac{M_{\text{prop}}}{\frac{1}{2} \rho A_i V_i r_{\text{prop}}^2}. \quad (11)$$

In “Eq. (11)”, M_{prop} represents the propeller torque, and r_{prop} is the radius of the propeller. The swirl velocity has a direct influence on the vertical component of the flap vanes’ velocity. Taking into account the previously mentioned V_e in both horizontal and vertical directions, it yields:

$$\mathbf{V}_e = \begin{bmatrix} u_e \\ v_e \\ w_e \end{bmatrix} = \begin{bmatrix} V_e \sin(\alpha_e) \\ 0 \\ V_e \cos(\alpha_e) \end{bmatrix}. \quad (12)$$

In “Eqs. (12)”, \mathbf{u}_e and \mathbf{w}_e represent the two components of the total outlet velocity, corresponding to the x and z axes, respectively. Introducing the flap vane velocity components in all three dimensions as $V_{f_{\text{v}}}$, we arrive at the following set of equations:

$$\begin{aligned} \mathbf{V}_{f_{\text{v}}} &= [u_{f_{\text{v}}} \ v_{f_{\text{v}}} \ w_{f_{\text{v}}}]^T, \\ \mathbf{V}_{f_{\text{v}}} &= \begin{bmatrix} 0 & 0 & -1 \\ -1 & 0 & 0 \\ 0 & 1 & 0 \end{bmatrix} \begin{bmatrix} \cos(\delta_{f_{\text{v}}}) & -\sin(\delta_{f_{\text{v}}}) & 0 \\ \sin(\delta_{f_{\text{v}}}) & \cos(\delta_{f_{\text{v}}}) & 0 \\ 0 & 0 & 1 \end{bmatrix} \end{aligned}$$

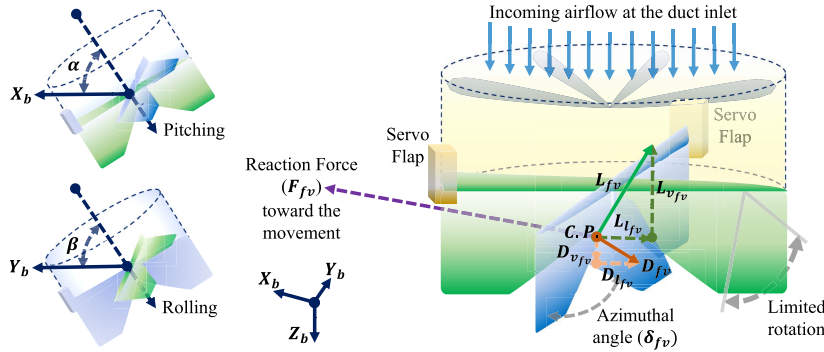


Fig. 7. Schematic of a duct with two pairs of flap vanes rotating, illustrating generated forces and reaction force.

$$\begin{aligned} & \times \begin{bmatrix} \mathbf{u}_e \cos(\delta_{fv}) \\ \mathbf{u}_e \sin(\delta_{fv}) \\ -\mathbf{w}_e \end{bmatrix} + \begin{bmatrix} 0 \\ 0 \\ r\omega_{\text{swirl}} \end{bmatrix}, \\ \rightarrow \mathbf{V}_{fv} = & \begin{bmatrix} \mathbf{u}_e \sin(\delta_{fv}) \\ -\mathbf{u}_e \cos(\delta_{fv}) \\ r\omega_{\text{swirl}} - \mathbf{w}_e \end{bmatrix} \quad (13) \end{aligned}$$

Equation (13) introduces three crucial variables: u_{fv} , v_{fv} , and w_{fv} , signifying the chordwise, spanwise, and normal constituents of the flap vane velocity. These variables derive their values from the influence of the outlet airstream exhaust emanating from the duct. The parameter δ_{fv} , equivalent to the vane's deflection angle or the widely acknowledged azimuthal angle ϕ , constitutes a pivotal aspect. This angle delineates the divergence between the vertical axis and the projection of the COP of the vane upon the horizontal plane. For an intricate depiction of the utilized flap vanes, refer to "Fig. 6". This illustrative diagram aptly showcases the three principal rotations imperative for generating roll, pitch, and yaw moments in the pursuit of optimal functionality.

Furthermore, the downwash angle induced by the duct is presented, which is usually negative due to the propeller that creates an airflow that is directed downward. It is also related to the lift force of the duct by the following expression:

$$\begin{aligned} \gamma_d &= \frac{\mathbf{F}_{\text{duct}}}{\dot{m}v_e}, \\ \gamma_d &= \begin{bmatrix} \gamma_{d_x} \\ \gamma_{d_y} \end{bmatrix} = \begin{bmatrix} \mathbf{F}_{\text{duct}}/(\rho\pi r^2((v_i - v_z)^2 + v_x^2)) \\ \mathbf{F}_x/(\rho\pi r^2((v_i - v_z)^2 + v_y^2)) \end{bmatrix}, \\ \mathbf{V}_{fv} &= \begin{bmatrix} u_{fv} \\ v_{fv} \\ w_{fv} \end{bmatrix} = \begin{bmatrix} u_{fv_p} & u_{fv_r} & u_{fv_y} \\ v_{fv_p} & v_{fv_r} & v_{fv_y} \\ w_{fv_p} & w_{fv_r} & w_{fv_y} \end{bmatrix}, \\ \delta_{fv} &= \begin{pmatrix} \alpha_{fv} \\ \beta_{fv} \\ \epsilon_{fv} \end{pmatrix} \end{aligned}$$

$$= \begin{pmatrix} \delta_{fv} + \arctan 2(-u_{fv_p} - v_{fv_p} l_{fv}, v_i - w_{fv_p}) \\ -\gamma_{d_x} - \delta_{fv} + \arctan 2(-v_{fv_r} - u_{fv_r} l_{fv}, v_i \\ - w_{fv_r}) - \gamma_{d_y} \\ \delta_{fv} + \arctan 2(-v_{fv_y} l_{fv}, v_i - w_{fv_y}) \end{pmatrix}. \quad (14)$$

In "Eq. (14)", the downwash angle (γ_d) is calculated based on the total duct thrust (as defined in "Eq. (8)", the mass airflow passing through the duct (refer to "Eq. (7)"'), and the exit velocity. This equation unveils the significant impact of the downwash angle on the final azimuthal angle of the flap vanes. In practical scenarios, such as the "WILD HOPPER" platform with a wide-diameter exhaust, the downwash angle deviates from the ideal conditions considered during the design process. This deviation carries implications, particularly for large-scale systems. Considering the three rotational angle axes for the vane azimuthal angle, we have α_{fv} (longitudinal direction), β_{fv} (lateral direction), and ϵ_{fv} (vertical direction). To account for the entire body's angular velocity, induced velocity (v_i) at the flap vane neighborhood is factored in. Additionally, the distance between the Center of Gravity (COG) of the MDF and the Center of Pressure (COP) of the flap vane (or their aerodynamic center), represented as l_{fv} , plays a crucial role in these calculations. For a more detailed discussion on these aspects, refer to [44]. The velocity of the flap vanes is expressed in "Eqs. (14)" as a 3×3 matrix, delineating each element corresponding to pitch ($\{\cdot\}_{fv_p}$), roll ($\{\cdot\}_{fv_r}$), and yaw ($\{\cdot\}_{fv_y}$) flap vanes.

As depicted in "Fig. 7", the incoming airflow is directed into a duct as the MDF moves along the longitudinal X -axis. Positioned near the duct's outlet, the two servo flaps exert control on the exhaust airflow, prompting a reactive response from the flap vanes to the exiting airflow. In this dynamic, a pair of forces emerge L_{fv} and D_{fv} , signifying the creation of Lift and Drag forces for each set of vane pairs. An important consideration is the azimuthal angle, δ_{fv} , which is restricted within the $\pm 15^\circ$ range to prevent interference

with adjacent cross-linked vanes. This precaution safeguards against potential disruptions. Furthermore, “Fig. 7” demonstrates two potential deflections of the single duct. The deflection corresponding to longitudinal movement is denoted as α , while the angle associated with lateral movement is designated as β . Moreover, the derived force acting on the flap is central to defining the flap force equation set, which can be expressed as follows:

$$\begin{aligned} \mathbf{L}_{\text{fv}} &= L_{l_{\text{fv}}} i + L_{v_{\text{fv}}} j = L_{\text{fv}} \cos(\delta_{\text{fv}}) i + L_{\text{fv}} \sin(\delta_{\text{fv}}) j, \\ \mathbf{D}_{\text{fv}} &= D_{l_{\text{fv}}} i + D_{v_{\text{fv}}} j = -D_{\text{fv}} \sin(\delta_{\text{fv}}) i + D_{\text{fv}} \cos(\delta_{\text{fv}}) j, \\ \mathbf{T}_{\text{fv}} &= L_{v_{\text{fv}}} i - D_{v_{\text{fv}}} j = \mathbf{L}_{\text{fv}} \sin(\delta_{\text{fv}}) - \mathbf{D}_{\text{fv}} \cos(\delta_{\text{fv}}), \\ \mathbf{F}_{\text{fv}} &= L_{l_{\text{fv}}} i + D_{l_{\text{fv}}} j = \mathbf{L}_{\text{fv}} \cos(\delta_{\text{fv}}) + \mathbf{D}_{\text{fv}} \sin(\delta_{\text{fv}}). \end{aligned} \quad (15)$$

Equation (15) presents the breakdown of the lift force into distinct lateral and vertical components, denoted as $L_{l_{\text{fv}}}$ and $L_{v_{\text{fv}}}$, respectively. Similarly, the drag force is divided into lateral and vertical components, represented by $D_{l_{\text{fv}}}$ and $D_{v_{\text{fv}}}$ for a flap vane. The aggregate thrust force produced by the flap vane, denoted as T_{fv} , results from combining the vertical components of both lift and drag forces. In contrast, the lateral force generated by the flap, marked as F_{fv} , arises from the summation of both lateral components of lift and drag forces. This interesting observation reveals that the lateral components of the decomposed lift and drag forces act in parallel, enhancing the MDF's forward momentum with increased force.

4.2. Advanced attitude controller

Having thoroughly examined the dynamics and mathematical modeling of the MDF platform, this section, alongside the subsequent one, succinctly encapsulates the essence of the control algorithm put forth in previous publications. The aim is to provide a comprehensive overview of the equations presented in the publications while grasping the underlying hypotheses. The overall control schematic for both methods is depicted in “Fig. 8”, encompassing several distinct packages as reference values presented x_r , y_r , z_r , and ψ_r ; position controller, vertical controller, attitude controller, Electric Control Unit (ECU), Servo Flap Dynamics (SFD), EDF Motor Dynamics (EDF-MD), secondary attitude dynamics, attitude dynamics, position dynamics, and disturbances. In this paper, we delve into the intricacies of the attitude controller, a crucial component responsible for stabilizing the UAV during flight maneuvers, including rotations and turns that induce transitional movements. The control of these movements is achieved through dedicated controller surfaces strategically positioned at the duct exits. These surfaces modulate the exhaust air to generate the requisite lift force, thereby influencing the UAV's azimuthal angle. Furthermore, the vertical controller, while constituting a segment of the position controller, operates

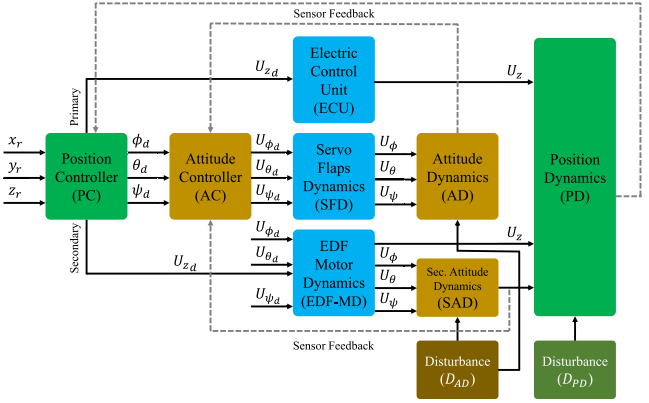


Fig. 8. Diagram illustrating the overarching control scheme implemented for precisely regulating the heavy hexa MDF system known as the “WILD HOPPER.”

independently of attitude angles. Termed the “vertical controller,” it plays a pivotal role in regulating the UAV's vertical movements. This section holds particular significance, representing a focal point in the authors' prior works, where it is expounded upon in greater detail in [8, 9].

Defining the state and input vectors, two approaches are evident: one based on the state values as followed in previous research, and the other aligned with state values utilized in studies concerning conventional DFs. In all scenarios, the input matrix remains consistent, as outlined below:

$$\begin{aligned} \mathbf{X} &= [x \dot{x} y \dot{y} z \dot{z} \phi \dot{\phi} \theta \dot{\theta} \psi \dot{\psi}]^T, \\ \mathbf{X}_{\text{alt}} &= [u \dot{u} w \dot{w} p \dot{p} q \dot{q} r \dot{r} \phi \dot{\phi} \theta \dot{\theta} \psi \dot{\psi}]^T, \\ \mathbf{U} &= [u_z u_\phi u_\theta u_\psi]^T. \end{aligned} \quad (16)$$

In “Eq. (16)”, \mathbf{X}_{alt} corresponds to an alternative state matrix formulation as defined in other research works. In this section, the second model is considered to align the control framework with established DF standards in [40–42, 45] to present an ASMC strategy against an array of external disturbances, such as wind gusts, fluctuations in payload weight, and uncertainties in dynamics, which makes it particularly appealing. In the context of a state-space representation involving an n th-order derivative of the system's state vector, the determination of the sliding surface is expressed as

$$\begin{aligned} x^{(n)} &= Ax + Bu + \delta(x) \rightarrow x^{(n)} = f(x) + u \\ \rightarrow S &= \left(\frac{d}{dt} + \lambda \right)^{(n-1)} (\dot{x} - \dot{x}_d) \rightarrow S = \left(\frac{d}{dt} + \lambda \right)^{(n-1)} e. \end{aligned} \quad (17)$$

In “Eq. (17)”, the symbol $\delta(x)$ denotes system uncertainties and nonlinearities encapsulated within the disturbance

function. It is assumed that δ remains within the bounds $\delta(x) < k$, where k is a positive constant representing the maximum anticipated disturbance magnitude. Additionally, the symbol λ represents the sliding surface gain or slope coefficient, determined based on the weighting of the uncertainties. The introduction of the sliding variable S

serves to quantify the tracking error, e , that emerges between the desired trajectory X_d and the actual trajectory X of the system. The overarching objective is to drive the sliding variable S towards zero, thereby aligning the actual state values with the desired state. In this specific scenario where $n = 2$ and it corresponds to a straightforward MDF system,

Controller Data

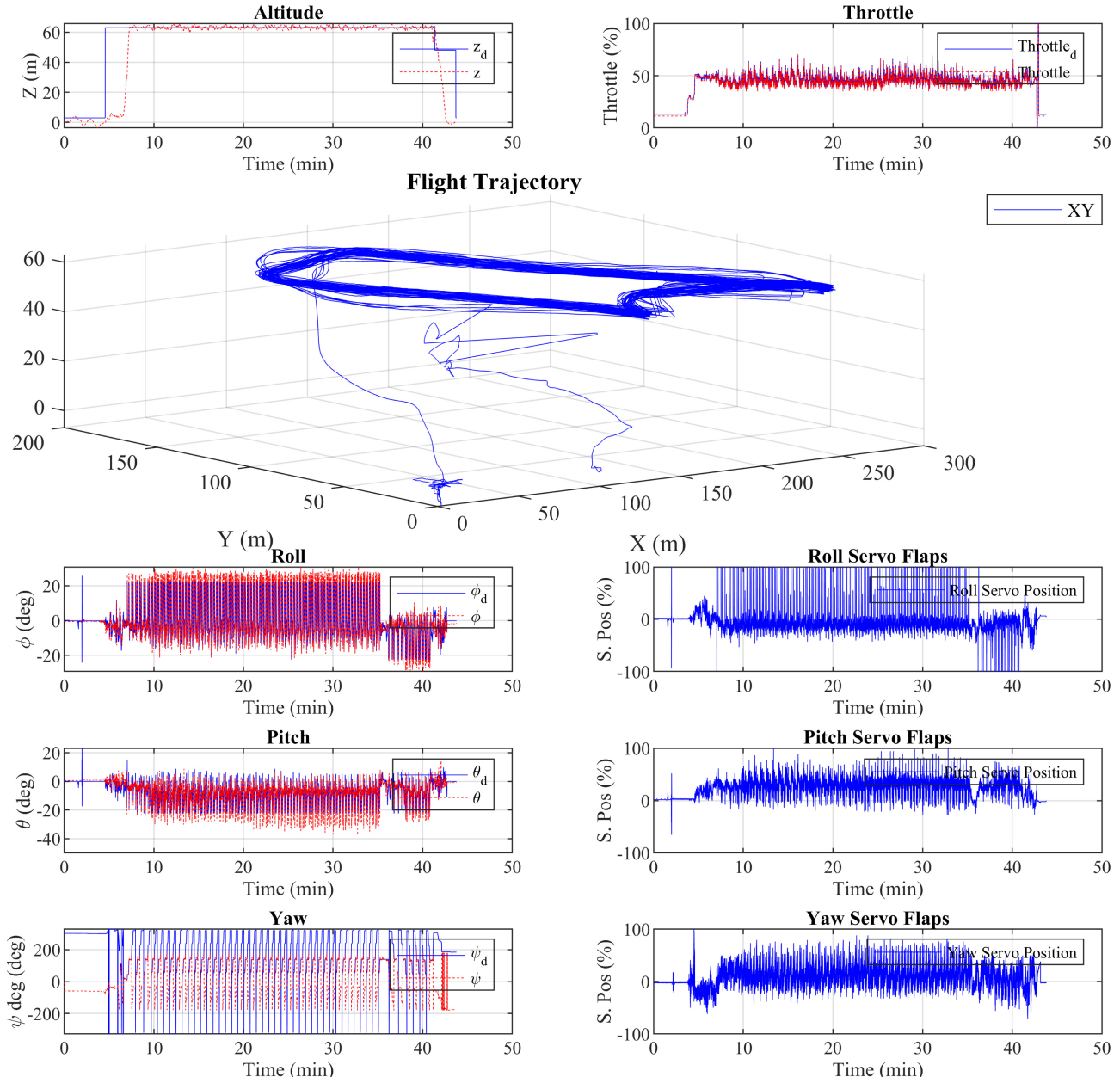


Fig. 9. Simulation: Attitude controller performance during a cruise flight, controlled by a cascade PID and utilizing flap vanes.

the formulation of the sliding surface is elaborated as follows:

$$S = \dot{e} + \lambda e = \dot{x} - \dot{x}_d + \lambda(x - x_d). \quad (18)$$

Indeed, a significant challenge within the SMC method lies in the careful definition of the sliding surface. However, one can assert that the sliding surface ideally mirrors the

system's error. This error signifies the disparity that necessitates a reduction to zero within the intended system.

$$\begin{aligned} \dot{S} &= \ddot{x} - \ddot{x}_d + \lambda(\dot{x} - \dot{x}_d), \\ \dot{x} = f(x) + u &\rightarrow u_{eq} : \dot{S} = 0 \rightarrow u_{eq} = X_d - \lambda \dot{e} \end{aligned} \quad (19)$$

In "Eqs. (19)", the u_{eq} stands for the equivalent control input, which is a part of the total control input specifically

Controller Data

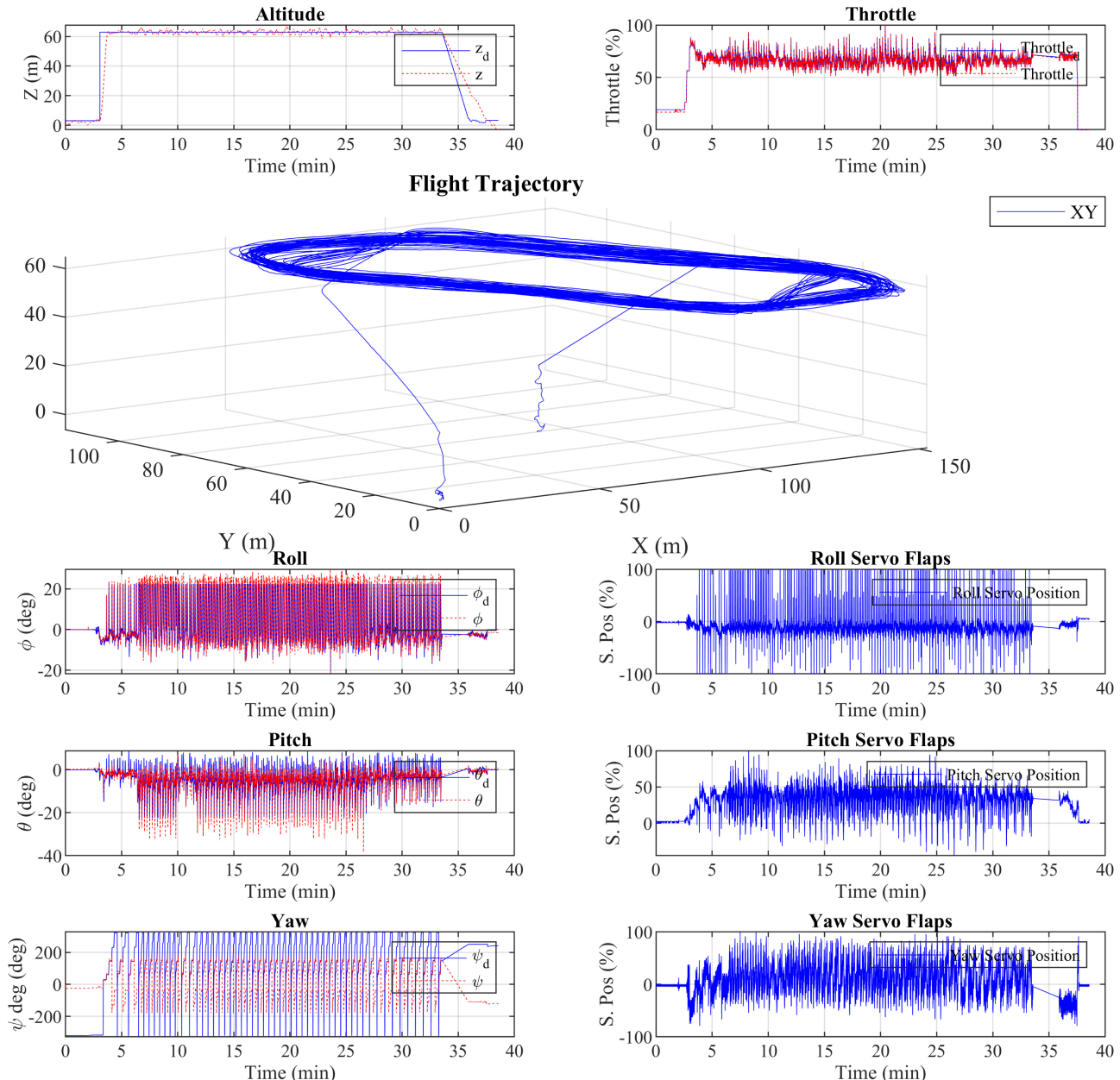


Fig. 10. Simulation: Attitude controller performance during a cruise flight, controlled by the presented robust controller and utilizing flap vanes.

designed to drive the system onto the sliding surface and maintains sliding mode behavior. As seen, the control input has appeared in the first derivative of the sliding variable. Therefore, the relative degree of the system is equal to 1. Moreover, the complete control input is defined, encompassing both the equivalent control input, denoted as u_{eq} , and the uncertain term of the system. This can be expressed as follows:

$$u = u_{eq} - d \times \text{sign}(s), \quad (20)$$

In "Eq. (20)", the term $\text{sign}(s)$ embodies the switching or uncertainty component within the control law. This term accommodates system uncertainties, external disturbances, or any unaccounted dynamics that could influence the system's behavior. Its purpose is to enhance the robustness of the control system when confronted with uncertain factors that might impact the system's performance. To determine the unknown parameter d , a Lyapunov candidate is introduced. This candidate is not only Positive-Definite (PD) itself but also has a Negative-Definite (ND) derivative, as shown in what follows. To mitigate the chattering phenomenon, which can cause undesirable high-frequency oscillations, the $\tanh(s)$ function is employed instead of the abrupt $\text{sign}(s)$ function. Additionally, for improved and swifter stability convergence, it is assumed that the derivative of the Lyapunov candidate is not only ND but also significantly more negative than a predefined positive value, μ . This choice ensures stability within a finite timeframe.

$$\begin{aligned} \text{updating : } & u = u_{eq} - d \times \tanh(s), \\ & V(x) = S^2/2 \rightarrow dV(x)/dt = ss, \\ \text{necessitates that : } & \dot{V}(x) \leq -\mu \rightarrow ss \leq -\mu|s| \\ \text{knowing that : } & s(x^{(n)}) = Ax + Bu + \delta(x) \\ & = s(-db \tanh(s) + \delta(x)) \quad (21) \\ \rightarrow & -db|s| + |s\delta(x)| = -db|s| + |s||\delta(x)| = \\ & |s|(-db + |\delta(x)|) \leq -\mu|s| \\ \rightarrow & -db + k \leq -\mu \rightarrow d \geq (\mu + k)/b. \end{aligned}$$

Hence, by adhering to the condition $d \geq (\mu + k)/b$, the stability of the system can be effectively ensured. This condition plays a pivotal role in bolstering the control system's ability to resiliently counter uncertainties and disturbances, thereby facilitating the achievement of both stability and precise tracking of the intended trajectory. Thus, in the context of the control law, the reformulation of the attitude controller concerning the azimuthal angle of the flap vanes can be expressed as

$$\begin{aligned} U_{roll} &= I_x(\ddot{\delta}_{fv_d} - k_1 \dot{e}_\phi) - k_1 \tanh(k_3 S), \\ U_{pitch} &= I_y(\ddot{\delta}_{fv_d} - k_2 \dot{e}_\theta) - k_1 \tanh(k_3 S), \quad (22) \\ U_{yaw} &= I_z(\ddot{\delta}_{fv_d} - k_3 \dot{e}_\psi) - k_2 \tanh(k_1 S). \end{aligned}$$

Table 1. Controller parameters fine-tuned for practical flight scenarios.

Parameter	Value
k_1	1.236
k_2	0.911
k_3	1.568
b	0.88
d	4.01

Table 2. Specification of the final Duty Hopper prototype.

Component	Parameter	Value	Dimension
Fuselage	Mass	350	Kg
	Height	163	cm
	Width	311	cm
	I_{xx}	411.62	Kg.m^2
	I_{yy}	411.62	Kg.m^2
	I_{zz}	536.31	Kg.m^2
	Number	4	—
Propeller	Blade Number	5	—
	Blade Radii	67	cm
	Blade Tip Chord	10	cm
	Blade Tip Angle	7.5	deg
	Nominal Rotor Rev.	1200	rpm
Propeller Duct	Thrust Factor	2.16e-2	N.m^2
	Length	37	cm
	Outer Diameter	151	cm
	Inner Diameter	155	cm
	Arc Radii at Tip	7	cm
Flap Vane	Avg. Inlet air Velocity	135	m/s
	Avg. Exit air Velocity	63.56	m/s
	Number	8	—
	Number per Prop	8	—
	Height	27	cm
Servo Flap	Length	53	cm
	Avg. Width	8	cm
	Max Azimuthal Angle	± 15	deg
	Number	4	—
	Avg. Speed	0.35	$\text{s}/60^\circ$
	Input Signal	200	Hz
	Rated Torque	150	Kg.s

By using "Eqs. (22)", the constants k_i with $i \in \{1, 2, 3\}$ will be determined through trial and error during the implementation phase. Ultimately, as a result of applying the control law, the attitude controller interfaces with the position controller.

5. Results

In previous works [8, 9, 30], simulation results of different adaptive and robust approaches were presented, compared

to a well-tuned PID controller and discussed that contributed to the enhancement of the dynamic model and controller solutions. This paper exclusively presents simulation results comparing the optimized SMC with a fine-tuned cascade PID system, thereby presenting a series of real-world results. These results focus on five of the most successful missions performed by the redesigned and fine-tuned Duty Hopper prototype. Previously, the initial schematic of this prototype was explored in detail in [30]. Through successive iterations and improvements, this model has recently reached Technology Readiness Level 7

(TRL-7), signifying its readiness for practical deployment. The specification of the final model is summarized in "Table 2". During the tests, the final configuration, which includes the payload weighing 350 Kg, features each duct equipped with a single primary propeller comprising five blades (as discussed in aerodynamics enhancements in [9]). Additionally, the flap vanes installed per duct are interconnected in pairs, as illustrated in "Fig. 6". Each flap series is actuated by a servo high-torque metal steering gear capable of applying moments of up to 400 kg.s. Consequently, for the desired quad DF configuration, eight sets of flap

Controller Data

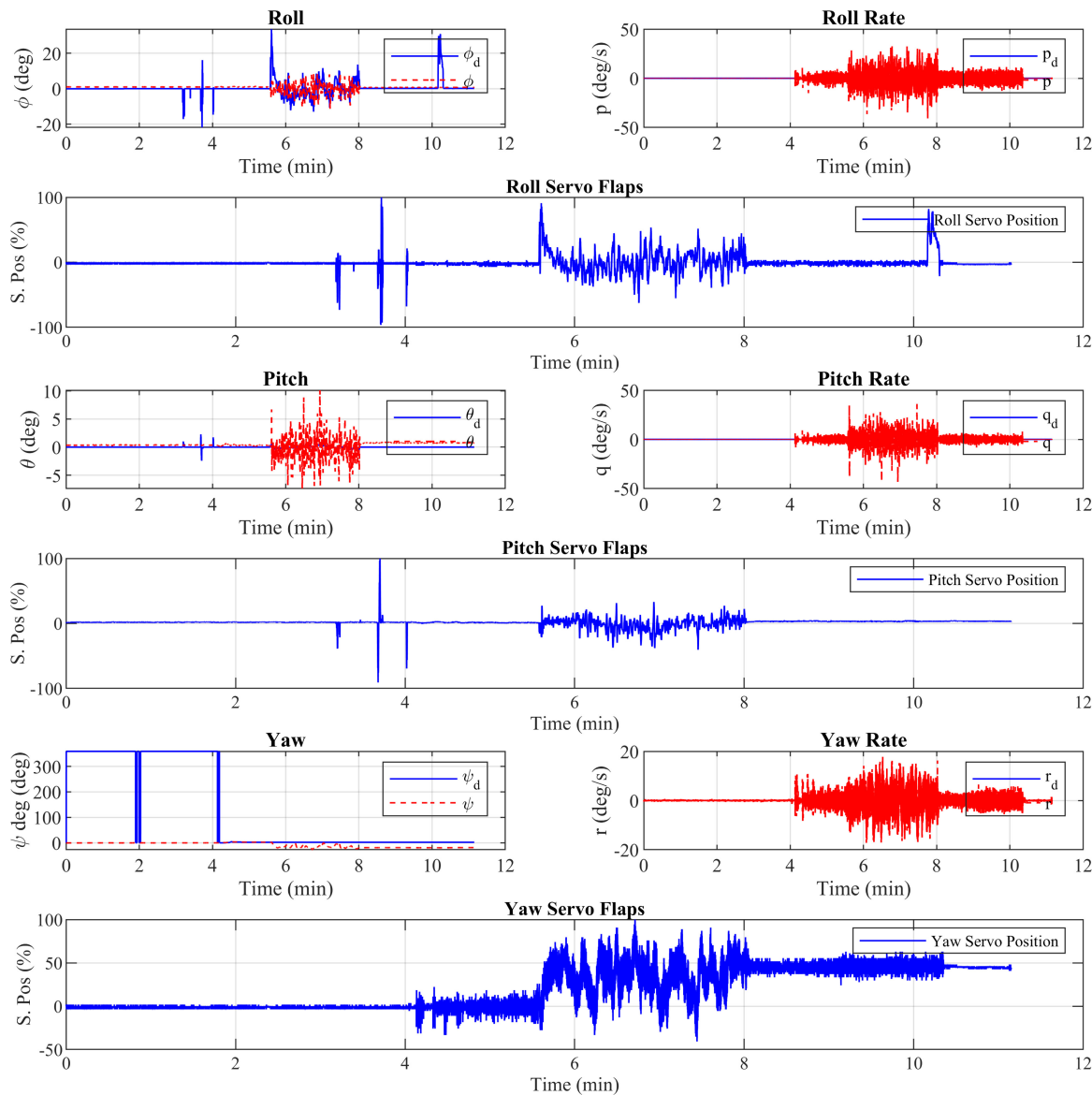


Fig. 11. Real Flight: Attitude controller performance during a hover flight, enhanced by TVC utilizing flap vanes to stabilize the system against uncertainties applied on the yaw loop.

vanes and four sets of servo flaps are deemed optimal for achieving peak performance.

5.1. Simulation results

Building upon previous research [9], the simulation process is conducted within the dynamic space of Gazebo on Ubuntu 18.04. The flap vanes joints were modeled as cylindrical bars connected to servo-simulated springs, incorporating presumed bandwidth and amplitude gain margins. Further

details about the codified components models are available in [8, 9]. In the subsequent analysis, two figures illustrate the outcomes of two cruise flights conducted by the heavy Wild Hopper model over approximately 40 minutes for comparison. Figure 9 showcases the controller performance of a finely tuned PID controller. The top part depicts the altitude compared to the desired altitude, revealing a noticeable but manageable error. On the right, the total thrust of all propellers is presented, while the 3D plot illustrates the drone's trajectory throughout the flight. Zooming in on the movements, a five-line polygon of waypoints was

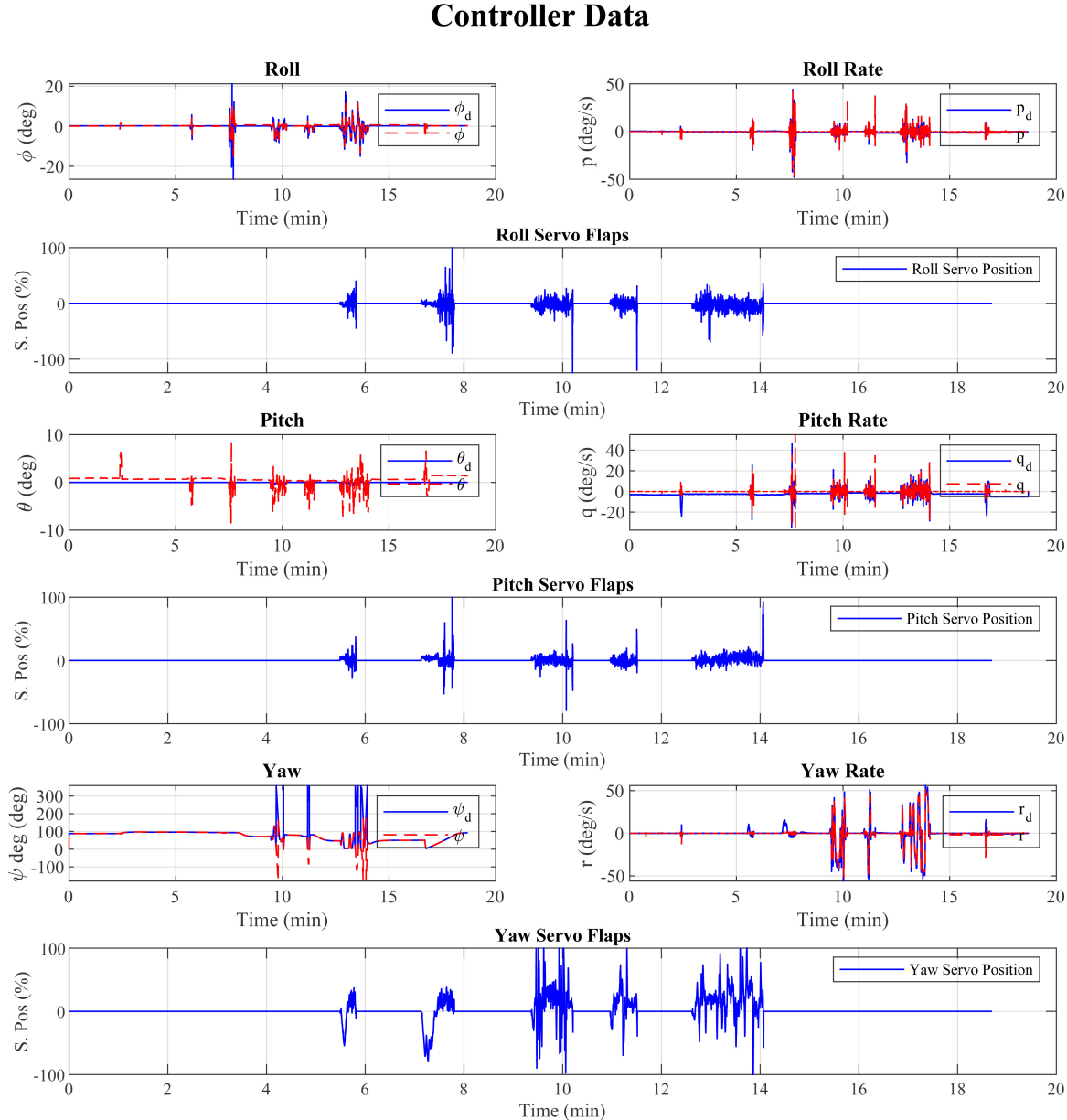


Fig. 12. Real Flight: Attitude controller performance during a hover flight, enhanced by TVC utilizing flap vanes to stabilize the system against uncertainties applied on the roll and pitch loops.

defined to observe attitude performance at turning points. Over time, trajectory errors accumulate in the integrator, especially at turning points. However, these errors diminished thanks to the cascade loop compensating for the deviated lines. Notably, some errors emerged during ascents since the waypoints were not horizontally aligned. This indicates that the PID controller struggled to stabilize effectively when altitude changes occurred simultaneously. Nevertheless, it demonstrated merely acceptable results during hover and cruise flights.

The second simulation flight utilized the robust method introduced in this paper. As depicted in “Fig. 10”, the overall flight trajectory mirrors that of the PID controller. In this simulation, a rectangular flight plan was initially executed. However, halfway through the flight, the rectangle underwent a 20-degree horizontal rotation to assess potential controller parameter accumulation. Remarkably, the controller effectively stabilized the flight, showcasing minimal attitude errors in the roll, pitch, and yaw loops. In contrast to the PID controller, this time the ascending phase was

Controller Data

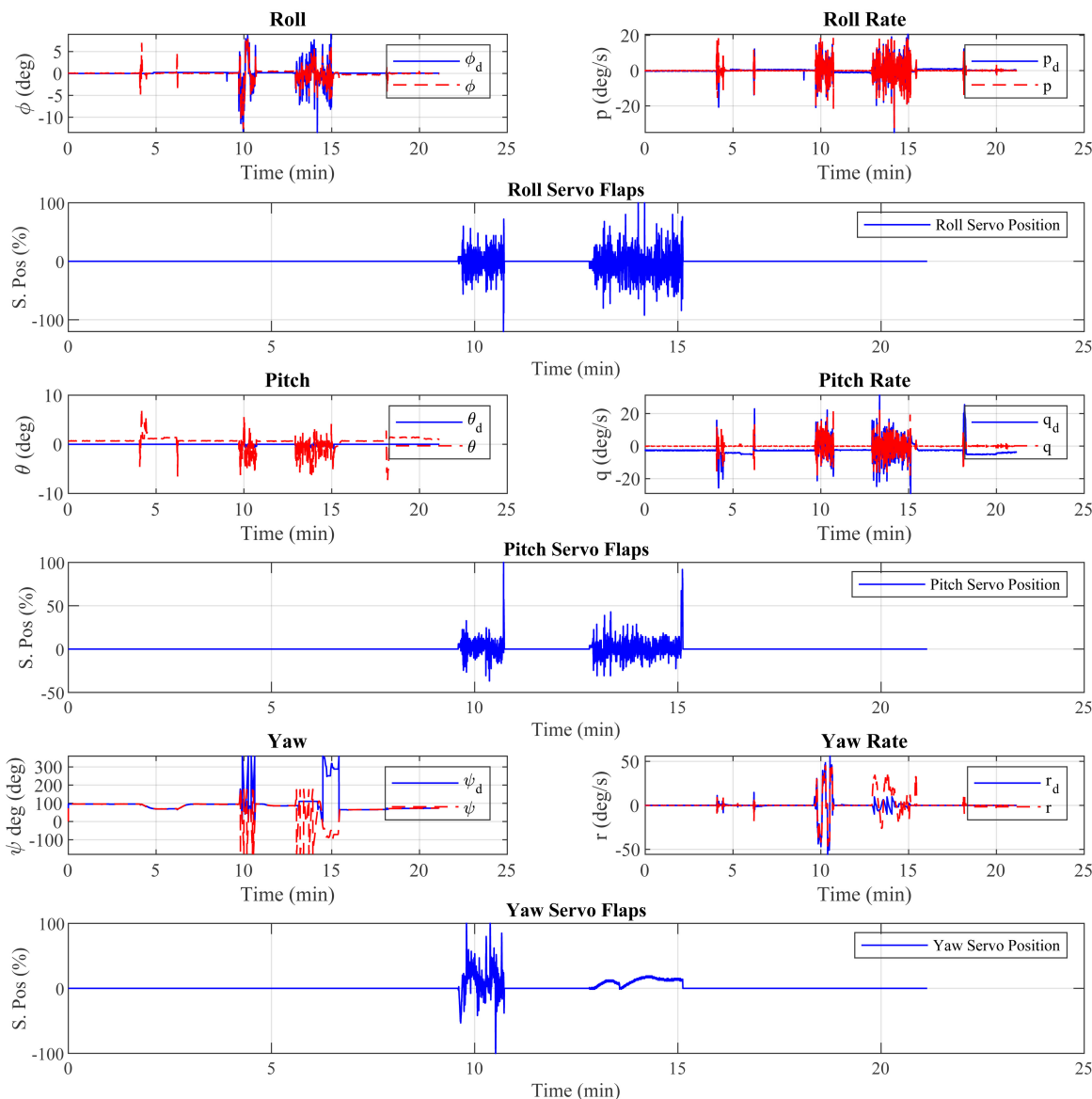


Fig. 13. Real Flight: Attitude controller performance during a cruise flight with a rectangular trajectory, enhanced by TVC utilizing flap vanes to stabilize the system against uncertainty applied on the roll and pitch loops.

more intense, and unexpectedly, moments of instability occurred during ascent that were beyond the controller's immediate control. However, the drone's swift movements effectively compensated for the instability, ensuring a safe landing.

5.2. Real-world flight experiments

Crucially, the practical tests incorporated the utilization of fine-tuned SMC parameters. These parameters were

meticulously adjusted to guarantee precise control and steadfast stability in real-world flight scenarios, as defined in "Eqs. (22)" and detailed in "Table 1".

Hence, the parameter values presented in "Table 1" align with the AP employed during the flights, known as the Micropilot with dual CPU capabilities. Prior to the flights, rigorous examinations of the attitude controller applied to the AP were performed under stationary conditions. To facilitate the integration of these parameters into the AP's primary control loop, special Extender licenses were

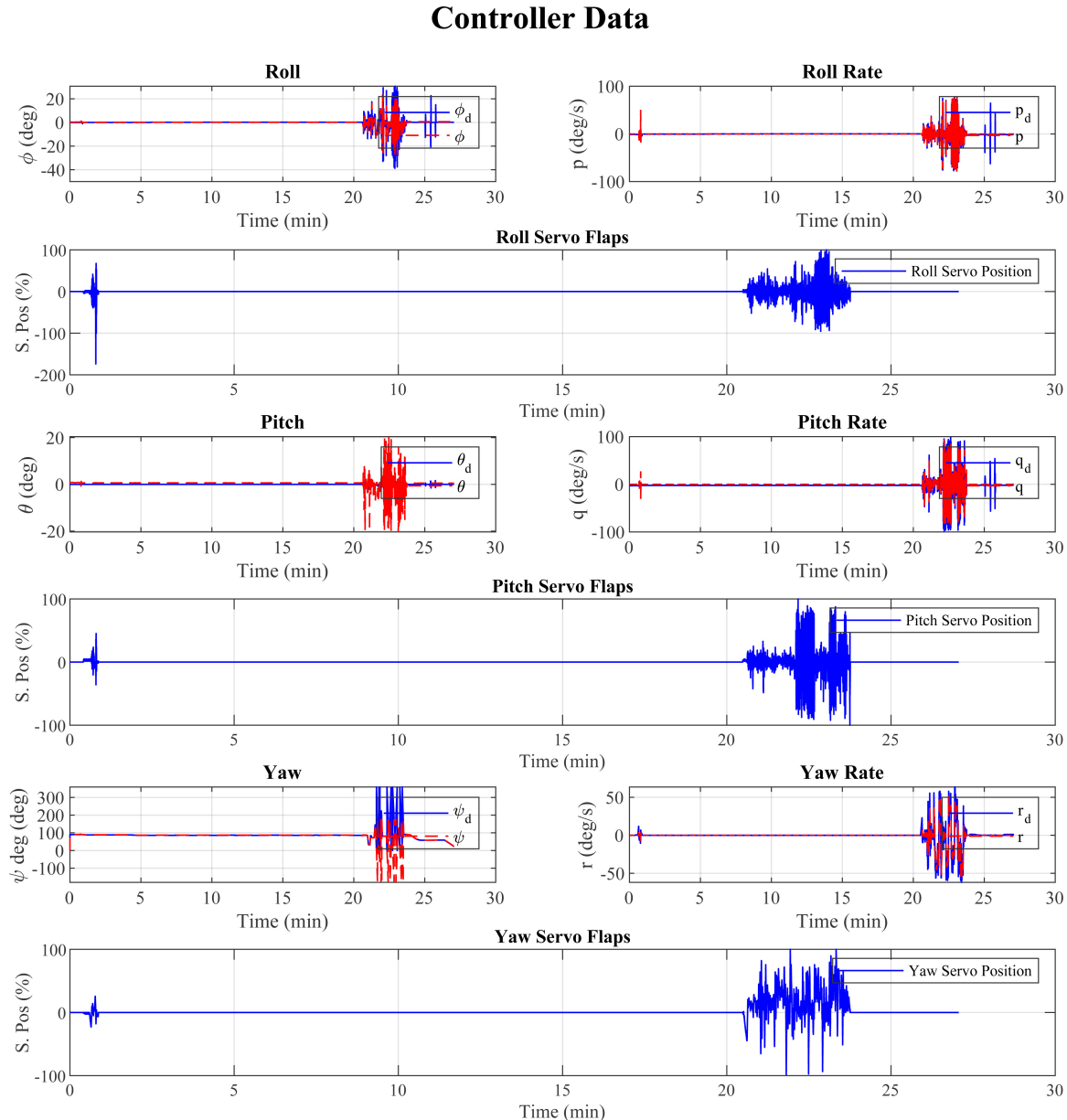


Fig. 14. Real Flight: Attitude controller performance during a cruise flight with a rectangular trajectory, enhanced by TVC utilizing flap vanes to stabilize the system against uncertainties applied on the yaw loop.

acquired, enabling the configuration of the firmware code and parameter adjustments through the Horizon user interface. Additionally, a simple plugin was developed within the application to facilitate parameter modification and tuning.

All the presented results share a common timeframe, with flight durations ranging from 11 to 27 min. These experiments primarily assess the efficiency of the attitude controller, with the position loop intentionally excluded from consideration. To aid clarity and ease of interpretation, we also include the rates of the Euler angles in our results, with a specific focus on the changes in roll, pitch, and yaw servo flap positions, presented in an comprehensive diagrams. Furthermore, it is important to note that the random noise equation employed for all flights remains consistent, as previously discussed in [9], and is consistently applied in the context of this research.

The first result illustrated in "Fig. 11", pertains to a brief hovering flight sequence. During this flight, we intentionally introduced random noise into the yaw controller loop for 60 ms, occurring in both the second and fourth minutes of the flight. The impact of this noise propagation is evident between the sixth and eighth minutes. However, as our diagrams vividly illustrate, the controller effectively managed this uncertainty, demonstrating its capability to stabilize the attitude even in the face of unexpected challenges.

The second flight, as shown in "Fig. 12", lasting approximately 19 min, featured two instances of random nonlinearity application during an almost hover flight, coupled with a few angle-turning trajectories. These nonlinearities were introduced once in the roll loop and once in the pitch loop. Notably, the overall system promptly re-established regulation. However, in the yaw loop, some interference became apparent due to accumulated errors introduced during the extended duration of the flight. In this instance, the adaptive parameters struggled to fine-tune the loop. Importantly, it is worth noting that the interference, while observable, remained within predefined limits as the yaw angle remained saturated.

The third flight, illustrated in "Fig. 13", comprised a 22-min cruise phase during which random noise was deliberately introduced into both the roll and pitch control loops. These uncertainties manifested as brief, 50-ms disturbances, with one occurring in the roll loop during the tenth minute and another in the pitch loop during the fifteenth minute of the flight. The results of this flight demonstrate the system's impressive recovery and adaptability, with adaptive parameters promptly adjusted before and during the flight to restore stability. This flight was extended to observe the assessment of accumulated errors in the yaw control loop. As depicted in the figure, the yaw rate effectively compensated for the nonlinearity, leading to a rapid decrease in yaw loop disturbances, highlighting the effectiveness of the system's adaptive capabilities.

The last flight, depicted in "Fig. 14", lasted for 27 min, following a rectangular trajectory. During the flight, a high noise was applied to the yaw loop precisely at the moment when the aircraft was making a turn within the rectangular path to evaluate the controller's performance under challenging conditions. As evident from the plots, the noise disturbance was applied at the 20th minute, leading to a response from the system that involved the coordinated use of both roll and pitch servo flaps. This cooperative action was necessary to counteract the nonlinearity observed in the system's behavior. Remarkably, the system successfully recovered within a minute, allowing the flight to continue without further issues.

6. Conclusions and Future Work

This paper consolidates three previous research efforts by the authors, introducing a novel controller state vector tailored for Multi-Ducted Fan (MDF) systems. The primary objective is to evaluate the effectiveness of an ARAC when applied to this specific system, employing a Thrust Vector Control (TVC) strategy through flap vanes and servo flaps at the duct's exhaust to regulate MDF attitude behavior. Brief dynamic equations are formulated to understand airflow dynamics, duct interaction, and the aerodynamic forces and moments involved in controller actuators. The controller's key concepts are outlined, and multiple flight tests assess its performance amid random disturbances, encompassing hover flights with roll, pitch, and yaw loop disturbances and cruise flights with attitude loop and servo flap disturbances. Outcomes demonstrate a satisfactory controller response in real flight scenarios, with the potential for further enhancements in industrial applications and varying temperature conditions. It is worth mentioning that TVC's adaptability and precise control make it an invaluable asset for heavy UAVs in various industrial settings to enhance maneuverability, improve stability, and the capability to counteract disturbances encountered during missions effectively. In future work, a focus will be placed on the enhancement of flap vane efficiency, with particular attention given to the optimization of their geometric profiles. The aim is to reduce drag and eliminate the need for auxiliary vanes, achieved through the integration of both lateral and longitudinal vane components, enabling the generation of yaw moments via diagonal vane rotation.

Acknowledgments

We would like to thank the University of Carlos III, campus Leganes, Madrid, for performing laboratories and hangers

through our research. We would also like to thank our colleagues at Drone Hopper for their support during the project. This work was conducted to complete the doctoral project of Mohammad Sadeq Ale Isaac with the support of Professor Pascual Campoy, and Doctor Ahmed Refaat Ragab. This work was supported by the ULTRADRON Project, funded by CDTI under the call number PTAP-20231017, focused on "Enabling Technologies for an Intelligent Logistics Unit with Drone Technology" and by the project INSERTION ref. ID2021-127648OBC32, "UAV Perception, Control and Operation in Harsh Environments," funded by the Spanish Ministry of Science and Innovation under the program "Projects for Knowledge Generating."

ORCID

- Mohammad Sadeq Ale Isaac  <https://orcid.org/0000-0001-8773-7184>
 Pablo Flores Peña  <https://orcid.org/0009-0005-7219-6879>
 Marco Andrés Luna  <https://orcid.org/0000-0003-1036-7538>
 Ahmed Refaat Ragab  <https://orcid.org/0000-0002-6897-6048>
 Pascual Campoy  <https://orcid.org/0000-0002-9894-2009>

References

- [1] K. L. N. C. Prakash, S. K. Ravva, M. Rathnamma and G. Suryanarayana, AI applications of drones, in *Drone Technology: Future Trends and Practical Applications* (Wiley, 2023), pp. 153–182.
 [2] Office of the Secretary of Defense, Unmanned aircraft systems roadmap: 2005–2030 (2005).
 [3] T. Elmokadem and A. V. Savkin, Towards fully autonomous UAVs: A survey, *Sensors* **21**(18) (2021) 6223.
 [4] S. A. H. Mohsan, N. Q. H. Othman, Y. Li, M. H. Alsharif and M. A. Khan, Unmanned aerial vehicles (UAVs): Practical aspects, applications, open challenges, security issues, and future trends, *Intell. Serv. Robot.* **16**(1) (2023) 109–137.
 [5] A. I. Abrego, R. W. Bulaga and M. Rutkowski, Performance study of a ducted fan system, *American Helicopter Society Aerodynamics, Acoustics and Test and Evaluation Technical Specialists Meeting* (California, USA, 2002).
 [6] A. Ko, O. Ohanian and P. Gelhausen, Ducted fan uav modeling and simulation in preliminary design, *AIAA Modeling and Simulation Technologies Conf. Exhibit* (2007), p. 6375.
 [7] L. González-deSantos, News applications of UAVs for infrastructure monitoring: Contact inspection systems, *Eng. Proc.* **17**(1) (2022) 23.
 [8] M. S. Ale Isaac, M. A. Luna, A. R. Ragab, M. M. Ale Eshagh Khoeini, R. Kalra, P. Campoy, P. Flores Peña and M. Molina, Medium-scale UAVs: A practical control system considering aerodynamics analysis, *Drones* **6**(9) (2022) 244.
 [9] M. S. Ale Isaac, A. R. Ragab, M. A. Luna, M. M. Ale Eshagh Khoeini and P. Campoy, Thrust vectoring control for heavy UAVS, employing a redundant communication system, *Sensors* **23**(12) (2023) 5561.
 [10] Y. Zeng, R. Zhang and T. J. Lim, Throughput maximization for UAV-enabled mobile relaying systems, *IEEE Trans. Commun.* **64**(12) (2016) 4983–4996.
 [11] V. U. Castrillo, A. Manco, D. Pascarella and G. Gigante, A review of counter-UAS technologies for cooperative defensive teams of drones, *Drones* **6**(3) (2022) 65.
 [12] M. Muehlebach and R. D'Andrea, The flying platform—a testbed for ducted fan actuation and control design, *Mechatronics* **42** (2017) 52–68.
 [13] N. Wang, S.-F. Su, M. Han and W.-H. Chen, Backpropagating constraints-based trajectory tracking control of a quadrotor with constrained actuator dynamics and complex unknowns, *IEEE Trans. Syst. Man, Cybern. Syst.* **49**(7) (2018) 1322–1337.
 [14] T. Manzoor, Z. Sun, Y. Xia and D. Ma, Mpc based compound flight control strategy for a ducted fan aircraft, *Aerosp. Sci. Technol.* **107** (2020) 106264.
 [15] D. Invernizzi and M. Lovera, Trajectory tracking control of thrust-vectoring UAVs, *Automatica* **95** (2018) 180–186.
 [16] M. Labbadi and M. Cherkaoui, Robust adaptive backstepping fast terminal sliding mode controller for uncertain quadrotor UAV, *Aerosp. Sci. Technol.* **93** (2019) 105306.
 [17] E. Tobias and J. Horn, Simulation analysis of the controllability of a tandem ducted fan aircraft, *AIAA Atmospheric Flight Mechanics Conf. Exhibit* (2008), p. 6700.
 [18] W. Fan, B. Xu, Y. Zhang, S. Tang and C. Xiang, Adaptive fault-tolerant control of a novel ducted-fan aerial robot against partial actuator failure, *Aerosp. Sci. Technol.* **122** (2022) 107371.
 [19] H. Jiang, Y. Zhou, H. W. Ho and W. Hu, Adaptive model predictive control for engine-driven ducted fan lift systems using an associated linear parameter varying model, *arXiv:2309.12552*.
 [20] Z.-H. Cheng and H.-L. Pei, Control effectiveness enhancement for the hovering/cruising transition control of a ducted fan UAV, *J. Intell. Robot. Syst.* **105**(4) (2022) 89.
 [21] Z. Cheng and P. Hailong, A corridor-based flight mode transition strategy for agile ducted-fan tail-sitter UAV: Altitude-hold transition, *Chin. J. Aeronaut.* **36**(9) (2023) 330–345.
 [22] M. Miwa, Y. Shigematsu and T. Yamashita, Control of ducted fan flying object using thrust vectoring, *J. Syst. Des. Dyn.* **6**(3) (2012) 322–334.
 [23] B. Xu, X. Wang, C. Xiang, Y. Ma and W. Chen, Modelling and hovering control of a novel multi-tandem ducted fan vehicle, *2015 Int. Conf. Unmanned Aircraft Systems (ICUAS)* (IEEE, 2015), pp. 1346–1354.
 [24] W. Fan, C. Xiang and B. Xu, Modelling, attitude controller design and flight experiments of a novel micro-ducted-fan aircraft, *Adv. Mech. Eng.* **10**(3) (2018), doi: 1687814018765569.
 [25] K. Feng, J. Ji, Y. Zhang, Q. Ni, Z. Liu and M. Beer, Digital twin-driven intelligent assessment of gear surface degradation, *Mech. Syst. Signal Process.* **186** (2023) 109896.
 [26] K. Feng, J. Ji, Q. Ni, Y. Li, W. Mao and L. Liu, A novel vibration-based prognostic scheme for gear health management in surface wear progression of the intelligent manufacturing system, *Wear* **522** (2023) 204697.
 [27] A. Townsend, I. N. Jiya, C. Martinson, D. Bessarabov and R. Gouws, A comprehensive review of energy sources for unmanned aerial vehicles, their shortfalls and opportunities for improvements, *Helion* **6**(11) (2020).
 [28] G. Wang, W. Samaratunga and S. Wang, Uninterruptible power supply design for heavy payload tethered hexarotors, *Int. J. Emerg. Eng. Res. Technol.* **4**(2) (2016) 16–21.
 [29] M. Adamski, Analysis of propulsion systems of unmanned aerial vehicles, *J. Marine Eng. Technol.* **16**(4) (2017) 291–297.

- [30] M. S. A. Isaac, A. R. Ragab, E. C. Garcés, M. A. Luna, P. F. Peña and P. C. Cervera, Mathematical modeling and designing a heavy hybrid-electric quadcopter, controlled by flaps, *Unmanned Syst.* **10**(3) (2022) 241–253.
- [31] J. Jeong, S. Kim and J. Suk, Control performance analysis on variable configuration of ducted-fan flight array, *Int. J. Aeronaut. Space Sci.* **21** (2020) 524–537.
- [32] S. B. F. Asl and S. S. Moosapour, Adaptive backstepping fast terminal sliding mode controller design for ducted fan engine of thrust-vec-tored aircraft, *Aerospace Sci. Technol.* **71** (2017) 521–529.
- [33] C. Chen, T. Dong, W. Fu and N. Liu, On dynamic characteristics and stability analysis of the ducted fan unmanned aerial vehicles, *Int. J. Adv. Robot. Syst.* **16**(4) (2019), doi: 1729881419867018.
- [34] J. Jeong *et al.*, Control system design for a ducted-fan unmanned aerial vehicle using linear quadratic tracker, *Int. J. Aerosp. Eng.* **2015** (2015) 364926.
- [35] J. Yu, A. Jadbabaie, J. Primbs and Y. Huang, Comparison of nonlinear control design techniques on a model of the caltech ducted fan, *Automatica* **37**(12) (2001) 1971–1978.
- [36] C. R. Kothari, *Research Methodology: Methods and Techniques* (New Age International, 2004).
- [37] A. T. Bahill and B. Gissing, Re-evaluating systems engineering concepts using systems thinking, *IEEE Trans. Syst. Man Cybern. C (Appl. Rev.)* **28**(4) (1998) 516–527.
- [38] B. W. Boehm, A spiral model of software development and enhancement, *Computer* **21**(5) (1988) 61–72.
- [39] S. Shan, Z. Hou and S. Wang, Controller design and experiment of the ducted-fan flying robot, *2016 IEEE Int. Conf. Robotics and Biomimetics (ROBIO)* (IEEE, 2016), pp. 1852–1857.
- [40] Y. Wang, C. Xiang, Y. Ma and B. Xu, Comprehensive nonlinear modeling and simulation analysis of a tandem ducted fan aircraft, in *Proc. 2014 IEEE Chinese Guidance, Navigation and Control Conf.* (IEEE, 2014), pp. 255–261.
- [41] W. Xiaoliang, C. Xiang, H. Najjaran and X. Bin, Robust adaptive fault-tolerant control of a tandem coaxial ducted fan aircraft with actuator saturation, *Chin. J. Aeronaut.* **31**(6) (2018) 1298–1310.
- [42] Y. Zhang, C. Xiang, B. Xu, X. Wang and W. Fan, Comprehensive non-linear modeling and attitude control of a novel tandem ducted fan vehicle, *2016 IEEE Int. Conf. Aircraft Utility Systems (AUS)* (IEEE, 2016), pp. 50–56.
- [43] H. Zhao, Development of a dynamic model of a ducted fan VTOL UAV, PhD thesis, RMIT University (2009).
- [44] E. N. Johnson and M. A. Turbe, Modeling, control, and flight testing of a small-ducted fan aircraft, *J. Guid. Control Dyn.* **29**(4) (2006) 769–779.
- [45] S. A. Emami and A. Banazadeh, Robustness investigation of a ducted-fan aerial vehicle control, using linear, adaptive, and model predictive controllers, *Int. J. Adv. Mechatron. Syst.* **6**(2–3) (2015) 108–117.



Mohammad Sadeq Ale Isaac received his M.S. and B.S. degrees from the University of Amirkabir, AUTMAV Laboraroy, and Khajenasi in 2019 and 2015, respectively. Currently, he is nearing completion of his PhD at the Centre for Automation and Robotics (CAR), Universidad Politécnica de Madrid (UPM-CSIC). He is the author of over 10 technical publications, proceedings, editorials, and books. Currently, he works in Wake-Eng as a flight dynamics engineer and ground control station visual interface software engineer. His research interests include Flight Dynamics, Nonlinear Control or UAVs, and Robotic Application topics.



Pablo Flores Peña is Aeronautical engineer and the CEO and CTO of the Drone Hopper Company, Madrid, Spain. He created the research center at Drone Hopper Company. Also, he holds IE MBA. He has more than 15 years of experience as Chief Engineer at Airbus Company.



Marco Andrés Luna is Ph.D. candidate at the Centre for Automation and Robotics (CAR), Universidad Politécnica de Madrid (UPM-CSIC) and SW engineer at Ahyres Company, Madrid, Spain. He obtained his B.S. degree in automation and control engineering from Universidad de las Fuerzas Armadas ESPE and his B.S. degree in automatic and robotics from the Polytechnic University of Madrid.



Ahmed Refaat Ragab is Postdoctoral Researcher at the University of Carlos III, and Drone Hopper Company, Madrid, Spain. He is a lecturer at October 6 University, Egypt. He was graduated from Air Defense College, Alexandria, Egypt. His field of interest is Unmanned Aerial Systems.



Pascual Campoy Cervera is Professor at the Higher Technical School of Industrial Engineers of the Polytechnic University of Madrid. He is the head of the research group “Vision for Unmanned Aerial Vehicles (UAVs)” of the Department of Automation, Electrical Engineering and Electronics and Industrial Informatics of the Centre for Automation and Robotics (CAR), Universidad Politécnica de Madrid (UPM-CSIC). The objective of his research group is to provide unmanned systems with greater autonomy through the use of computer vision techniques.